https://doi.org/10.5194/wes-2025-288
Preprint. Discussion started: 9 January 2026

eawe european academy of wind energy
Open Access WIND ENERGY SCIENCE DISCUSSIONS

Large eddy simulation of airborne wind energy systems flying in turbulent wind using model predictive control

Jean-Baptiste Crismer[1], Thomas Haas[2], Matthieu Duponcheel[1], and Grégoire Winckelmans[1]

[1]Institute of Mechanics, Materials and Civil Engineering (iMMC), Université catholique de Louvain (UCLouvain), 1348 Louvain-la-Neuve, Belgium
[2]Thermodynamics and Fluid Mechanics (FLOW), Faculty of Engineering, Vrije Universiteit Brussel (VUB), 1050 Brussels, Belgium

Correspondence: Jean-Baptiste Crismer (jean-baptiste.crismer@uclouvain.be)

Abstract. Wind energy is foreseen to be a cornerstone of the future energy mix, with a total capacity projected to increase drastically in the coming decades. To this end, the size of horizontal-axis wind turbines is continuously increasing, which poses significant structural challenges and requires increasing material resources. Those challenges have triggered interest in alternative technologies. Airborne wind energy (AWE) shows great potential and has recently gained a great deal of interest. However, the implementation of airborne wind energy systems (AWES) is in its infancy, and the only existing systems operate isolated. For AWES to take an active part in wind energy, their operation in turbulent environments must be further studied, and wind farms must also be considered. This work proposes a framework based on computational fluid dynamics for studying AWES in ambient turbulent wind and wakes, as will be encountered when arranged in farms. The present work focuses on ground-gen rigid-wing AWES. The framework relies on a large eddy simulation flow solver, in which the kites are represented using a model based on an actuator line for the main wing with its ailerons, and complemented with models for the tail control surfaces (rudder and elevator). The flow solver is coupled, via a two-way coupling, to a control module based on model-predictive control, to follow optimal trajectories. The framework is presented in some detail and is then used to investigate the MegAWES aircraft, a MW-scale AWES of 42.5 m wingspan, here flying four-loop trajectories. The first part of the investigation focuses on a single system. Its ability to fly in a turbulent wind is demonstrated and analyzed, and its wake is also characterized. It is demonstrated that the controlled kite can handle the turbulent wind. The deviation from its reference trajectory is less than 15% of the wingspan. In the second part, a tandem configuration is considered, with the same foor-loop trajectory for each kite. It is found that there is a configuration where the second kite, even fully aligned with the first one, can fly in unperturbed flow (other than the turbulence of the wind). A second case is investigated where the second kite is forced to fly in the wake from the first one. It is found that the wake produced by the first kite does not compromise the trajectory tracking of the second kite. However, the second kite feels the velocity deficit and its power production is reduced by 6%.

1 Introduction

Wind energy is considered a cornerstone to achieve the energy transition. The worldwide total installed capacity is expected to be multiplied by eight by 2050 to meet the net zero emission scenario (IEA – International Energy Agency, 2021). Horizontal

https://doi.org/10.5194/wes-2025-288
Preprint. Discussion started: 9 January 2026

eawe european academy of wind energy
Open Access WIND ENERGY SCIENCE DISCUSSIONS

axis wind turbines (HAWTs) are the most common technology to harness wind energy. Over the past few decades, their size has continuously increased in an effort to reduce the levelised cost of energy (Sørensen and Larsen, 2023). However, building ever-larger turbines introduces significant challenges, such as logistical difficulties with large components, increased structural stresses, blade bending, and the need for more robust foundations. These challenges have led to growing interest in exploring alternative technologies. A large list of future emerging technologies is provided in (Watson et al., 2019).

Among these, airborne wind energy (AWE) has attracted significant research interest over the past two decades because of its advantages compared to conventional wind energy systems. The concept of AWE was first theorized by Loyd in the 1970s. One of the major advantages of this technology lies in its low material requirements. The absence of a tower is itself an advantage, but it also allows for lighter foundations, resulting in a lower overall carbon footprint (Hagen et al., 2023). A second key advantage is its ability to easily reach high altitudes, taking advantage of higher velocity winds, and adjust its altitude based on the wind strength (Bechtle et al., 2019).

The technology relies on tethered wings, i.e., kites. A wide range of concepts exists (Cherubini et al., 2015), but the present work focuses on fixed-wing, lift-based airborne wind energy systems (AWES). These are aircraft-type systems for which the generator is on the ground. It is one of the most studied concepts. Its operation consists of pumping cycles that comprise two distinct phases. To generate energy, the kite flies in crosswind loops and maximizes the pulling force on its tether. The tether unwinds from a drum that is connected to a generator to produce electricity. This is the “reel-out phase”. When that phase ends, the tether is rewound on the drum; the so-called “reel-in phase”. The kite is put in a configuration such that it exerts the minimum required traction on the tether, allowing it to be retrieved using the generator as a motor. The device studied is the reference rigid-wing AWES from Eijkelhof and Schmehl (2022). The system and its operation are depicted in Fig. 1.

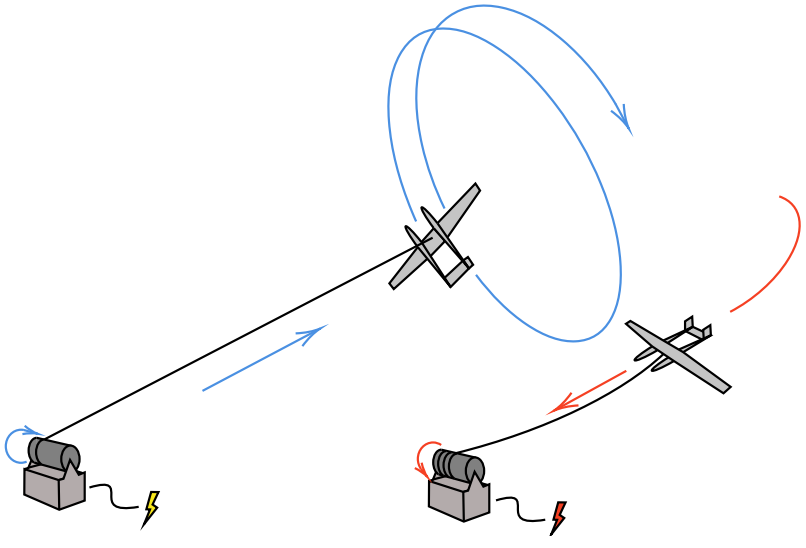

Figure 1. Ground-gen airborne wind energy system operating phases: reel-out (left) and reel-in (right) phases. Inspired from (Joshi et al., 2024).

https://doi.org/10.5194/wes-2025-288
Preprint. Discussion started: 9 January 2026

eawe european academy of wind energy
Open Access WIND ENERGY SCIENCE DISCUSSIONS

Much of the research conducted on AWES is about control and optimal path determination. Indeed, an AWES can move freely in space within a given set of constraints. The trajectory determines the energy yield of the system and is a first challenge that constitutes a vast research field (Eijkelhof and Schmehl, 2022; De Schutter et al., 2023; Vermillion et al., 2021). The second challenge is to be able to fly the computed/optimized trajectory, as this will directly affect the system performances. This becomes even more challenging when one considers the flow unsteadiness present in atmospheric flows (such as the wind turbulence, the wind shear, gusts); and also when one considers crossing the wake generated by another device (i.e. another AWES when considering a farm of AWESs (Haas et al., 2022), or even a HAWT when considering AWES added to a farm of HAWTs. Therefore, it is of prime importance to understand how these devices interact with complex and realistic flows. This is a key aspect to go towards the industrial implementation of AWESs and their operation in wind farms.

To properly study an AWES, many different building blocks must be put together. The main elements are the ground station, the tether, the kite itself with its dynamics, its aerodynamics and structural deformations, and the flow field. Each of those blocks is modeled with different levels of fidelity. While Vermillion et al. (2021) proposes a review of the different existing models, they focus on dynamics and control. Pynaert et al. (2023) proposed a first sorting of the different fidelity levels, also considering aero-elasticity in addition to aerodynamics.

Most studies focusing on developing kite simulators, or more generally on control and optimal trajectory, opt for simplified aerodynamic models (Sánchez-Arriaga et al., 2019; Eijkelhof and Schmehl, 2022; Rapp et al., 2019; De Schutter et al., 2023). They often rely on stability derivatives models or lookup tables, and use six degrees of freedom (DOF) dynamics models. Such aerodynamic models are based on an analytical formulation of the kite responses to certain flow conditions and kite configuration and motion. They are fast and already provide a pretty good estimate of the forces acting on the device. They are mainly used for preliminary design and optimization, when the force distribution on the wing is not required. Although more complex aerodynamic models for rigid-wing AWES exist, studies are still quite scarce; here are a few examples. Vimalakanthan et al. (2018) presents a study involving lifting line methods used for power prediction. Those methods are further used to evaluate the wing deformation by Wijnja et al. (2018), but only cover steady state scenarios. The actuator line (AL) method has been used to represent kites as well (Haas et al., 2022; Crismer et al., 2024). The lifting device is also represented by a line, but the surrounding flow is computed using a computational fluid dynamics (CFD) flow solver. Flow unsteadiness can therefore be accounted for. Fasel et al. (2019) used a 3D panel method to investigate the potential of morphing kites. CFD simulations using Reynolds averaged Navier–Stokes (RANS) equations were performed by Vimalakanthan et al. (2018) in steady configurations. Other studies use more advanced aerodynamic models in dynamic situations. The simpler dynamic situations consider prescribed circular trajectories. Haas and Meyers (2017) and Crismer et al. (2023) present studies of AWES wakes using LES in which the wing is modeled with an actuator line. Pynaert et al. (2022) present a study in which the kite's wing is fully modeled in a wing resolved unsteady RANS (URANS) simulation. More advanced dynamic situations, such as prescribed trajectories corresponding to complete power cycles, are presented in the work of Haas et al. (2019) and Pynaert et al. (2024), still using LES and URANS, respectively. It should be noted that Pynaert et al. (2024) also further refined their kite model to incorporate the control surfaces. The first investigations involving a kite controlled in a CFD simulation were

https://doi.org/10.5194/wes-2025-288
Preprint. Discussion started: 9 January 2026

eawe european academy of wind energy
Open Access WIND ENERGY SCIENCE DISCUSSIONS

carried out by Haas et al. (2022). More recently, Pynaert et al. (2024) and Crismer et al. (2024) also built a framework to perform such simulations.

As stated above, considering the inflow encountered by an AWES is of significant importance to move towards real systems operation. Concerning the wind, the accuracy lies in the modeling of the wind velocity profile, which varies with the altitude, and its unsteadiness and turbulence. A large part of the research in the field only considers the mean (i.e., time-averaged) wind profile of the atmospheric boundary layer (ABL). Yet, the following studies, using more sophisticated models, are worth mentioning: Sommerfeld et al. (2023) considered several steady wind profiles obtained from measurements to build a more realistic power curve prediction for AWES; Schelbergen et al. (2020), established a methodology to translate field measurements into a representative set of wind profiles to estimate the annual energy production of AWE systems; Rapp et al. (2019) assessed the robustness of their controller flying in a turbulent boundary layer pre-generated using large eddy simulation (LES). Using CFD, earlier studies considered steady uniform inflow (Pynaert et al., 2022) or turbulent uniform inflow (Haas and Meyers, 2017; Crismer et al., 2023, 2024), generated by the addition of synthetic turbulence to a uniform inflow. However, this neglects the variation of the wind velocity with altitude. Further refinement of the wind model leads to the use of a steady logarithmic wind velocity profile (Pynaert et al., 2023, 2024) in RANS simulation. The most realistic wind model used so far in the context of AWES simulations in the ABL is found in the work by Haas et al. (2022), which employs a concurrent precursor LES simulation of a pressure-driven boundary layer (PDBL). This method produces both realistic boundary layer profile and turbulence, however thermal effects and atmospheric stratification are not included.

The study by Haas et al. (2022) combines realistic wind modeling, actuator-based AWES representation, model-based trajectory optimization, and closed-loop optimal control within a single framework. The ABL flow is emulated using an LES simulation of a turbulent PDBL. Within the LES, only the main wing of the AWES is modeled using an actuator sector representation. The actuator sector method (ASM) combines the temporally-weighted contributions of an actuator line over the area swept by the wing. The dynamics of the wing is modeled using a 3DOF point-mass model, which provides the states and control variables required to compute the translational motion of the wing. With this model, flight path optimization and closed-loop control by means of Nonlinear Model Predictive Control (NMPC) are performed using the optimal control toolbox `AWEbox` (De Schutter et al., 2023). The system motion during closed-loop path tracking is driven by the aerodynamics forces computed using the 3DOF model, considering wind measurements from the LES. This framework is then used to simulate wake interaction and power performance of large farms of utility-scale AWESs in turbulent wind conditions.

The present work aims to introduce an LES-based aero-servo simulation framework similar to Haas et al. (2022), but employing refined models for the system dynamics and aircraft aerodynamics. To this end, the kite dynamics is represented using a 6-DOF model, while the wing aerodynamics is described using an Actuator Line (AL) approach. To compute the aerodynamic moments required by the 6-DOF model, the influence of the control surfaces is incorporated into the AL representation of the main wing. This results in a complete aircraft model. The control surface models are based on their geometry and lift slope coefficient. A two-way coupling between the AL-based model and the NMPC module of `AWEbox` allows closed-loop control flight simulations. Here, the system motion is therefore driven by the aerodynamic forces directly obtained from the AL-based

https://doi.org/10.5194/wes-2025-288
Preprint. Discussion started: 9 January 2026

eawe european academy of wind energy
Open Access WIND ENERGY SCIENCE DISCUSSIONS

model in the LES. The kite trajectories are generated with the `AWEbox`. The framework is subsequently utilized to compare system performance between idealized conditions in `AWEbox` and turbulent wind conditions.

This paper builds upon previous work (Crismer et al., 2024), further detailing the framework developed and extending it to more realistic trajectories. Furthermore, the framework is used to investigate the case of a single kite and the case of two kites in tandem, where the second one flies just behind the first one.

The tools and building blocks of the framework are presented in Sect. 2. A study of the AL accuracy is reported in Sect. 3. Section 4 details the numerical setup and the parameters used. The results obtained for the different investigated cases are presented and discussed in Sect. 5. Finally, conclusions are presented in Sect. 6.

2 Methodology

This section presents the different components of the framework. The flow solver is first introduced in Sect. 2.1. The system dynamics is described in Sect. 2.2. The aircraft model is then discussed in Sect. 2.4. Finally, `AWEbox`, which is used for trajectory generation and control, is presented in Sect. 2.5.

2.1 Flow solver

An LES approach combined with realistic modeling of the AWES (using an improved AL method for the wing and added modeling of the control surfaces: ailerons, rudder and elevator) is used here. We use LES because it allows for an accurate modeling of the flow turbulence and unsteadiness, and is therefore well suited to represent realistic wind.

The LES solver is based on fourth-order finite-differences for incompressible flows. It was developed at UCLouvain (Duponcheel et al., 2014; Moens and Chatelain, 2022). The Navier-Stokes equations are solved in their velocity-pressure formulation, truncated by the LES grid size, and supplemented with a subgrid-scale (SGS) model

$$\nabla \cdot \boldsymbol{v} = 0 \tag{1a}$$

$$\frac{\partial \boldsymbol{v}}{\partial t} + (\boldsymbol{v} \cdot \nabla)\boldsymbol{v} = -\nabla P + \nu \nabla^2 \boldsymbol{v} + \nabla \cdot \boldsymbol{\tau}^{\mathrm{SGS}} + \boldsymbol{f} \tag{1b}$$

where $\boldsymbol{v}$ is the velocity field, t is the time, $P = p/\rho$ is the kinematic pressure field, $\nu = \mu/\rho$ is the kinematic viscosity of the fluid. $\boldsymbol{\tau}^{\mathrm{SGS}}$ is the SGS stress tensor (also divided by ρ). It is modeled using the Regularized Variational Multiscale (RVM) model (Jeanmart and Winckelmans, 2007; Cocle et al., 2009). The volumetric forcing term $\boldsymbol{f}$ is used to represent the effect of AWESs. The domain is discretized using a cartesian staggered grid. The temporal integration is handled using the second-order Adams-Bashforth scheme.

The turbulent inflow consists of either synthetic turbulent fluctuations generated using the Mann algorithm (Mann, 1994) and added to the mean wind, or a neutral atmospheric boundary layer (ABL) obtained using a co-simulation (Trigaux et al., 2024a; Moens and Chatelain, 2022).

We stress that the LES solver, combined with improved AL modeling, has already been used in previous studies relating to wind energy. For instance, it was used to investigate the blade flexibility effects on the loads and wake of the very large IEA

https://doi.org/10.5194/wes-2025-288
Preprint. Discussion started: 9 January 2026

eawe european academy of wind energy
Open Access WIND ENERGY SCIENCE DISCUSSIONS

15 MW horizontal-axis wind turbine in (Trigaux et al., 2024a). The investigations included both cases of turbulent wind, using a Mann box (hence no mean shear) and using an ABL running as a LES co-simulation (hence also with mean wind shear).

In the present study, the kite flies relatively far from the ground, and the mean wind shear encountered by the kite is moderate. It was hence decided to neglect wind shear and the wall, and to use Mann boxes, those being pre-generated using `Hipersim` (Dimitrov et al., 2024).

2.2 AWES dynamics

When the kite flies with the controller, the dynamics is handled using the dynamics model from `AWEbox` (De Schutter et al., 2023), which is a modeling and optimization toolbox for AWES. The AWES can be decomposed into three main components: the ground station, which hosts the generator; the tether; and the kite. In the system model, the ground station is not modeled and the kite is directly controlled using the tether jerk (third derivative of the tether length). The tether is assumed to be a straight rod of varying length, going from the ground station to the kite center of gravity (CG) and subjected to drag only. Finally, the kite itself is modeled using a 6-DOF model for its dynamics subject to forces and moments. The computation of the forces and moments is handled using the actuator line and the control surfaces models within the flow solver, as presented in Sect. 2.4.

Two coordinate systems come into play to describe the system dynamics. The origin of the inertial coordinate system is placed at the ground station with the x-axis in the flow direction, the z-axis pointing upward, and the y-axis sideways to form a right-hand coordinate system. The body coordinate system origin is located at the CG of the kite with the x-axis pointing backward, the y-axis pointing starboard and the z-axis pointing upward, as shown in Fig. 2. The kite position in the inertial frame is described by its coordinates $\boldsymbol{q}$. The orientation of the kite in this reference frame is represented using a rotation matrix $\mathbf{R} \triangleq [\boldsymbol{e}_{x,b}, \boldsymbol{e}_{y,b}, \boldsymbol{e}_{z,b}]^T$ that contains chord-wise, spanwise and upwards unit vectors of the aircraft body frames, expressed in the inertial frame $\{\boldsymbol{e}_{x,I}, \boldsymbol{e}_{y,I}, \boldsymbol{e}_{z,I}\}$, and transforms the different vectors from the inertial frame to the kite body frame.

The kite state vector is the concatenation of the kite position $\boldsymbol{q}$, translational velocity $\dot{\boldsymbol{q}}$, rotational velocity $\boldsymbol{\omega}$, orientation described by the rotation matrix $\mathbf{R}$, control surfaces deflection $\boldsymbol{\delta}$, which is the concatenation of $[\delta_a, \delta_e, \delta_r]$ (ailerons, elevator and rudders actuation angles, respectively) and the tether length l, tether velocity $\dot{l}$, and tether acceleration $\ddot{l}$, and is therefore defined as

$$\boldsymbol{x} \triangleq \left(\boldsymbol{q},\, \dot{\boldsymbol{q}},\, \boldsymbol{\omega},\, \mathbf{R},\, \boldsymbol{\delta},\, l,\, \dot{l},\, \ddot{l}\right). \tag{2}$$

The control variables of the system are contained in the vector

$$\boldsymbol{u} \triangleq \left(\dot{\boldsymbol{\delta}},\, \dddot{l}\right) \tag{3}$$

and is a concatenation of the control surfaces actuation rates and the tether jerk.

https://doi.org/10.5194/wes-2025-288
Preprint. Discussion started: 9 January 2026

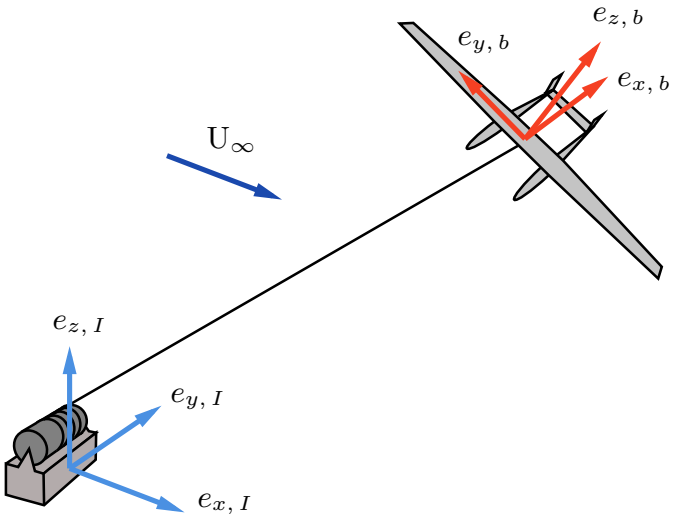

Figure 2. The airborne wind energy system and the reference frames.

The equations of motion of the kite are derived from Lagrangian mechanics (Gros and Diehl, 2013; De Schutter et al., 2023), and is expressed as

$$m\ddot{\boldsymbol{q}} - \lambda \boldsymbol{q} = \mathbf{R}^T \boldsymbol{F}_{e,b} - \overline{m}\, g\, \boldsymbol{e}_{z,I} \tag{4a}$$

$$\ddot{c} + 2\kappa_t \dot{c} + \kappa_t^2 c = 0 \tag{4b}$$

$$\mathbf{J}\dot{\boldsymbol{\omega}} + \boldsymbol{\omega} \times \mathbf{J}\boldsymbol{\omega} = \boldsymbol{M}_{e,b} \tag{4c}$$

$$\frac{d}{dt}\mathbf{R} = \mathbf{R}\left(\frac{\kappa_R}{2}\left(I - \mathbf{R}^T\mathbf{R}\right) - \mathtt{skew}(\boldsymbol{\omega})\right). \tag{4d}$$

Equation 4a corresponds to the translational kinematics, in which $m = (m_K + \frac{1}{3}m_T)$ and $\overline{m} = (m_K + \frac{1}{2}m_T)$ are the effective inertial and effective gravitational masses (Houska and Diehl, 2007) (with m_K and m_T the mass of the kite and of the tether, respectively), $\boldsymbol{F}_{e,b}$ is the external forces expressed in the body frame, g is the gravitational acceleration, and λ the Langrangian multiplier inherent to the chosen formulation. The translational kinematics is constrained with Eq. 4b in which $c = \frac{1}{2}(\boldsymbol{q}^T\boldsymbol{q} - l^2) = 0$ is the constraints that forces the kite to navigate on a hemisphere of radius equal to the tether length, and κ_t a constant stabilizing parameter. It is the Baumgarte stabilized form of the latter constraint c. Equation. 4c refers to the rotational kinematics, in which $\mathbf{J}$ is the kite inertia matrix, and $\boldsymbol{M}_{e,b}$ the external moments. A similar stabilization is used to guarantee the orthogonality of the rotation matrix. Equation 4d both describes the evolution of the rotation matrix and guarantee its orthogonality $\boldsymbol{c}_R = \mathbf{R}^T\mathbf{R} - I = 0$. In this equation κ_t another constant stabilizing parameter, and $\mathtt{skew}$ an operator that transforms a vector into the corresponding skew-symmetric matrix. Such stabilization also requires the initial constraint $C(\boldsymbol{x_0}) = (c(\boldsymbol{x_0}), \dot{c}(\boldsymbol{x_0}), \boldsymbol{c}_R(\boldsymbol{x_0})) = 0$. The interested reader can find more details on the dynamics formulation in Gros and Diehl (2013) and De Schutter et al. (2023).

https://doi.org/10.5194/wes-2025-288
Preprint. Discussion started: 9 January 2026

eawe european academy of wind energy
Open Access WIND ENERGY SCIENCE DISCUSSIONS

The system dynamics are integrated in time using a fourth order Runge-Kutta scheme:

$$\dot{\boldsymbol{x}} = \frac{d\boldsymbol{x}}{dt} = \left(\dot{\boldsymbol{q}},\, \ddot{\boldsymbol{q}},\, \dot{\boldsymbol{\omega}},\, \dot{\mathbf{R}},\, \dot{\boldsymbol{\delta}},\, \dot{l},\, \ddot{l},\, \dddot{l}\right). \tag{5}$$

The external forces $\boldsymbol{F}_{e,I} = \mathbf{R}^T \boldsymbol{F}_{e,b}$ applied to the system are the aerodynamic forces. The aerodynamic forces consist of the aerodynamic forces acting on the kite and the tether drag. Their evaluation is described in the following sections.

2.3 Tether model

The tether drag is evaluated assuming the drag coefficient $C_{D,T} = 1.2$ for a circular cross-section. The total drag on the tether is shared between the ground station and the kite, as detailed in De Schutter et al. (2023). The contribution that acts on the kite is evaluated by integrating along the tether using the coordinate $s \in [0, 1]$. An infinitesimal tether fragment therefore has a length $dl = l\, ds$ and the integral writes

$$\boldsymbol{F}_{D_T} = \int_0^1 s\left(\frac{1}{2}\rho \|\boldsymbol{v}_{a,t}(s)\| \boldsymbol{v}_{a,t}(s)\, C_{D,T}\, d_T\right)(l\, ds) \tag{6}$$

where $\boldsymbol{v}_{a,t}(s)$ is the apparent velocity projected perpendicularly to the tether and d_T is the tether diameter. The factor s in front of the parentheses is introduced to weight the fraction of the total drag that acts on the kite. The other part acts on the ground station. The integration is required because the drag force is not constant along the tether, as the apparent velocity varies along its length. In AWEbox, the integration is performed numerically by dividing the tether into n elements. Here, $n = 5$.

2.4 Kite AL model and models for the effect of the control surfaces

The aerodynamic forces that act on the kite are taken from the flow solver AL model. In this model, the main wing of the kite is modeled using an actuator line (AL) model, as in (Sørensen and Shen, 2002), and that line is immersed in the flow solver; meaning that it moves relatively to the fixed cartesian grid of the flow solver.

Capturing the effects of the turbulence on the kite requires that the flow solver grid size be sufficiently fine relative to the wingspan of the kite. It must therefore be sufficiently fine everywhere in the region of the flow domain through which the kite moves.

The AL method involves three main steps: flow velocity sampling, forces and moments evaluation, forces projection into the fluid. The AL is discretized into a set of N segments, at the center of each of which lies a control point. These control points are used as reference locations for the three main operations of the method. Knowing the position and orientation of the wing, the AL is placed along the quarter-chord line, and the positions of the control points are determined. For each control point, the local flow velocity is evaluated by performing a weighted average of the flow velocity in the vicinity of the control point. Once the velocity is known, the aerodynamic forces and moments are computed on the basis of airfoil polar data. Finally, the forces are projected onto the mesh surrounding the corresponding control point. They are accounted for by the flow solver through the volumetric force term on the right-hand side of Eq. (1b). Velocity sampling and force distribution are performed by means of a 2D Gaussian regularization kernel. Indeed, 2D kernels have been shown to be more accurate in predicting aerodynamic

https://doi.org/10.5194/wes-2025-288
Preprint. Discussion started: 9 January 2026

eawe european academy of wind energy
Open Access WIND ENERGY SCIENCE DISCUSSIONS

forces than the 3D kernel Caprace et al. (2020). In practice, a planar grid with its associated weights, referred to as a template, is placed at each control point, perpendicular to the AL. Linear interpolation is then used to transfer information from the template to the flow solver grid, and vice versa. More details on the implementation of the AL method can be found in Trigaux et al. (2024a, b).

This work considers the rigid-wing reference AWES called MegAWES (Eijkelhof and Schmehl, 2022). It has a wingspan of 42.5 m and a main wing aspect ratio of 12. The complete geometry considered in the present work is detailed in Appendix A. The geometry is slightly adapted to solve inconsistencies and simplify some parts.

The elevator and the two rudders are modeled as flat plates hinged about their aerodynamic center (i.e., at their quarter-chord). Owing to their low aspect ratio, these control surfaces are not well suited for an AL representation. Moreover, their dimensions are small relative to affordable grid resolution of the flow solver, which prevents an adequate spatial discretization. Their force contribution is therefore modeled analytically as ($\diamond \in [e, r]$)

$$L_\diamond = \frac{1}{2}\rho \|\boldsymbol{v}_{a,\diamond}\|^2 A \left.\frac{dC_L}{d\alpha}\right|_\diamond \alpha_\diamond \tag{7}$$

where A is the control surface area, $\left.\frac{dC_L}{d\alpha}\right|_\diamond$ is its effective lift slope coefficient and $\alpha_\diamond$ is the angle of attack of the measured apparent velocity relative to the chord. The lift slope coefficients were evaluated using a lifting surface method, thus properly taking into account the low aspect ratio of the control surface and the wake vorticity produced by it. As these estimates closely match those obtained from the Helmbold approximation for low aspect-ratio wings, the latter is adopted, yielding values of $1.01, \pi$ for the elevator and $0.50, \pi$ for the rudders.

The apparent velocity $\boldsymbol{v}_{a,\diamond}$ is obtained from the kite velocity and the local flow velocity. The flow velocity is interpolated at the aerodynamic center of each control surface using an $M'4$ kernel (Monaghan, 1985). The resulting aerodynamic loads are added to the forces acting on the body, with the resulting moments. Because these loads are small compared to those generated by the main wing, their impact on the flow field is neglected (i.e., we neglect the small wake vortices that they produce), and their influence is restricted to the body dynamics.

Aileron effects are incorporated directly within the actuator-line framework by adjusting the local airfoil characteristics according to the aileron deflection angle δ_a. For the i^{th} wing section of chord c_i, the lift per unit span is expressed as

$$l_i(\alpha) = \frac{1}{2}\rho \|\boldsymbol{v}_{a,i}\|^2 c_i \left(C_l(\alpha) + p_i \left((\eta\tau) \left.\frac{dC_l}{d\alpha}\right|_a \delta_a \right) \right) \tag{8}$$

where τ is the aileron effectiveness factor which depends on the fraction of the chord spanned by the aileron, c_a/c_i (here equal to 0.6), and $\eta = \eta(\delta_a)$ is a correction factor to account for the reduced aileron effectiveness as the deflection angle increases, see (McCormick, 1995). The lift slope of the ailerons $\left.\frac{dC_l}{d\alpha}\right|_a$ is that of the aerodynamic profile at its zero-lift angle. The contribution of an aileron to an AL control point is weighted proportionally to the fraction p_i that it spans on that AL segment. The influence of the ailerons is thus taken into account in the computation of the force distribution over the wing. A schematic of the whole AL-based kite model is depicted in Fig. 3.

https://doi.org/10.5194/wes-2025-288
Preprint. Discussion started: 9 January 2026

eawe european academy of wind energy
Open Access WIND ENERGY SCIENCE DISCUSSIONS

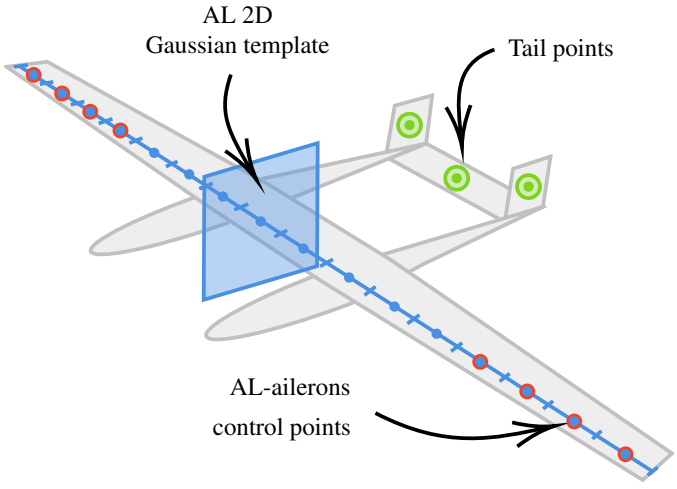

Figure 3. Schematic of the kite model with the actuator line model, including the ailerons, for the main wing and the evaluation points for the elevator and rudders models

It should be noted that, due to the variation of the wing properties (chord, twist, presence of ailerons), the number of AL control points must be chosen so that it can capture those characteristics.

2.5 Reference trajectories and control

The power output of an AWES is determined by its trajectory. It also depends on how well the kite can follow the planned trajectory. In the present work, the kite flies so-called "optimal trajectories" in the sense that the reference trajectories are generated through an optimization process performed using `AWEbox` (De Schutter et al., 2023). This is presented in Sect. 2.5.1. The controller is then used to fly these pre-computed optimal trajectories in the turbulent wind using flight path tracking. The control strategy is introduced in Sect. 2.5.2.

2.5.1 Optimal trajectories

`AWEbox` generates optimal trajectories by solving optimal control problems (OCP). In this case, we want to find a reference trajectory for the following optimization variables : the states $\boldsymbol{x}(t)$, the control input $\boldsymbol{u}(t)$, the algebraic variable $z(t) = \lambda$, a set of system constant parameters $\boldsymbol{p}$ and the trajectory time period T_p. Note that some system design parameters can also be optimized, such as the tether diameter; in our case, it is prescribed as a system parameter.

The trajectory is to be optimized so that it minimizes a cost function over the trajectory period. It takes into account the total power output, as well as a penalty on the use of the actuators, side-slip and angular acceleration, in order to prevent actuator fatigue and aggressive maneuvers. The penalty function $\hat{w}(t) \triangleq (\boldsymbol{u}, \beta(t), \dot{\omega}(t))$ is associated with weights $\mathbf{W}$. The optimization

https://doi.org/10.5194/wes-2025-288
Preprint. Discussion started: 9 January 2026

eawe european academy of wind energy
Open Access WIND ENERGY SCIENCE DISCUSSIONS

is constrained by the system dynamics, as described in Sect. 2.2 and summarized as

$$\boldsymbol{F}\left(\dot{\boldsymbol{x}}(t), \boldsymbol{x}(t), \boldsymbol{u}(t), z(t), \boldsymbol{p}\right) = 0, \tag{9}$$

and a set of constraints $\boldsymbol{h}$ that ensures that the system operation remains within acceptable bounds to preserve the hardware. The trajectory must also remain periodic, and the whole problem therefore reads

$$\min_{\boldsymbol{x}(t), \boldsymbol{u}(t), \lambda(t), T_p} \quad \frac{1}{T_p} \int_0^{T_p} \left(-P(t) + \hat{w}(t)^T \mathbf{W} \hat{w}(t)\right) dt \tag{10a}$$

$$\text{s.t.} \quad \boldsymbol{F}\left(\dot{\boldsymbol{x}}(t), \boldsymbol{x}(t), \boldsymbol{u}(t), \lambda(t), \boldsymbol{p}\right) = 0, \quad \forall t \in [0, T_p] \tag{10b}$$

$$\boldsymbol{h}\left(\dot{\boldsymbol{x}}(t), \boldsymbol{x}(t), \boldsymbol{u}(t), \lambda(t), \boldsymbol{p}\right) \leq 0, \quad \forall t \in [0, T_p] \tag{10c}$$

$$\boldsymbol{x}(0) - \boldsymbol{x}(T_p) = 0. \tag{10d}$$

For the optimization, the aerodynamic forces and moments must be given in the form of analytical expressions. The simplified internal aerodynamic model (Malz et al., 2019) is used and is formulated as follows

$$\boldsymbol{F}_a = \frac{1}{2}\rho \|\boldsymbol{v}_a\|^2 S \begin{bmatrix} C_x\left(\alpha, \beta, \boldsymbol{\omega}, \delta_{a,e,r}\right) \\ C_y\left(\alpha, \beta, \boldsymbol{\omega}, \delta_{a,e,r}\right) \\ C_z\left(\alpha, \beta, \boldsymbol{\omega}, \delta_{a,e,r}\right) \end{bmatrix}, \quad \boldsymbol{M}_a = \frac{1}{2}\rho \|\boldsymbol{v}_a\|^2 S \begin{bmatrix} b\, C_l\left(\alpha, \beta, \boldsymbol{\omega}, \delta_{a,e,r}\right) \\ \bar{c}\, C_m\left(\alpha, \beta, \boldsymbol{\omega}, \delta_{a,e,r}\right) \\ b\, C_n\left(\alpha, \beta, \boldsymbol{\omega}, \delta_{a,e,r}\right) \end{bmatrix} \tag{11}$$

where S is the wing surface, $\boldsymbol{v}_a$ is the apparent wind velocity, α is the aircraft angle of attack and β its side-slip angle (all measured at CG). The associated sub-coefficients are

$$\begin{bmatrix} C_x \\ C_y \\ C_z \end{bmatrix} = \begin{bmatrix} C_{x_0} \\ C_{y_0} \\ C_{z_0} \end{bmatrix} + \begin{bmatrix} C_{x_\beta} \\ C_{y_\beta} \\ C_{z_\beta} \end{bmatrix} \beta + \begin{bmatrix} C_{x_{\omega_x}} & C_{x_{\omega_y}} & C_{x_{\omega_z}} \\ C_{y_{\omega_x}} & C_{y_{\omega_y}} & C_{y_{\omega_z}} \\ C_{z_{\omega_x}} & C_{z_{\omega_y}} & C_{z_{\omega_z}} \end{bmatrix} \begin{bmatrix} b\,\omega_x \\ \bar{c}\,\omega_y \\ b\,\omega_z \end{bmatrix} \frac{1}{2\|\boldsymbol{v}_a\|^2} + \begin{bmatrix} C_{x_{\delta_a}} \\ C_{y_{\delta_a}} \\ C_{z_{\delta_a}} \end{bmatrix} \delta_a + \begin{bmatrix} C_{x_{\delta_e}} \\ C_{y_{\delta_e}} \\ C_{z_{\delta_e}} \end{bmatrix} \delta_e + \begin{bmatrix} C_{x_{\delta_r}} \\ C_{y_{\delta_r}} \\ C_{z_{\delta_r}} \end{bmatrix} \delta_r \tag{12a}$$

$$\begin{bmatrix} C_l \\ C_m \\ C_n \end{bmatrix} = \begin{bmatrix} C_{l_0} \\ C_{m_0} \\ C_{n_0} \end{bmatrix} + \begin{bmatrix} C_{l_\beta} \\ C_{m_\beta} \\ C_{n_\beta} \end{bmatrix} \beta + \begin{bmatrix} C_{l_{\omega_x}} & C_{l_{\omega_y}} & C_{l_{\omega_z}} \\ C_{m_{\omega_x}} & C_{m_{\omega_y}} & C_{m_{\omega_z}} \\ C_{n_{\omega_x}} & C_{n_{\omega_y}} & C_{n_{\omega_z}} \end{bmatrix} \begin{bmatrix} b\,\omega_x \\ \bar{c}\,\omega_y \\ b\,\omega_z \end{bmatrix} \frac{1}{2\|\boldsymbol{v}_a\|^2} + \begin{bmatrix} C_{l_{\delta_a}} \\ C_{m_{\delta_a}} \\ C_{n_{\delta_a}} \end{bmatrix} \delta_a + \begin{bmatrix} C_{l_{\delta_e}} \\ C_{m_{\delta_e}} \\ C_{n_{\delta_e}} \end{bmatrix} \delta_e + \begin{bmatrix} C_{l_{\delta_r}} \\ C_{m_{\delta_r}} \\ C_{n_{\delta_r}} \end{bmatrix} \delta_r \tag{12b}$$

where b is the wingspan and $\bar{c} = S/b$ its mean chord. Each coefficient $C_{\_,\_}$ of Eqs. (12a) and (12b) is modeled using a second order polynomial that depends on the angle of attack α. Those sub-coefficients were evaluated using the whole AL kite model and imposing the corresponding displacement or actuation. More details are provided in Appendix C.

https://doi.org/10.5194/wes-2025-288
Preprint. Discussion started: 9 January 2026

eawe european academy of wind energy
Open Access WIND ENERGY SCIENCE DISCUSSIONS

2.5.2 Control strategy

The kite flies the generated trajectory in a turbulent environment emulated by the LES. To guarantee that the kite stays on the desired trajectory, it has to be associated with a controller. In `AWEbox`, the flight path tracking is performed using non-linear model predictive control (NMPC). The model is the same as that used for trajectory optimization as described in previous sections. At each call of the controller, for a given state $\boldsymbol{x}_i$ and knowing the reference trajectory $\boldsymbol{x}_{\mathrm{ref}}$, the controller computes the best possible control actions in order to stick to the reference path. The prediction is done for a given time horizon T_h. For each prediction, an OCP is formulated (De Schutter et al., 2023)

$$\min_{\boldsymbol{x}(t),\boldsymbol{u}(t),z(t)} \quad \frac{1}{T_h}\int_0^{T_h} \left(\|\boldsymbol{x}(t)-\boldsymbol{x}_{\mathrm{ref}}(t)\|^2_{Q_C}+\|\boldsymbol{u}(t)-\boldsymbol{u}_{\mathrm{ref}}(t)\|^2_{R_C}\right) dt \tag{13a}$$

$$\text{s.t.} \quad \boldsymbol{F}\left(\dot{\boldsymbol{x}}(t),\boldsymbol{x}(t),\boldsymbol{u}(t),z(t),\boldsymbol{p}\right)=0, \quad \forall t\in[0,T_h] \tag{13b}$$

$$\boldsymbol{h}\left(\dot{\boldsymbol{x}}(t),\boldsymbol{x}(t),\boldsymbol{u}(t),z(t),\boldsymbol{p}\right)\leq 0, \quad \forall t\in[0,T_h] \tag{13c}$$

$$\boldsymbol{x}_0=\hat{\boldsymbol{x}}_0 \tag{13d}$$

$$\boldsymbol{x}(T_h)=\boldsymbol{x}_{\mathrm{ref}}(T_h). \tag{13e}$$

The objective is to minimize a cost function associated with the root mean square error of the actual course compared to the reference, Eq. (13a). The objective associated constraints are the kite dynamics Eq. (13b) and system bounds Eq. (13c), similarly to Eq. (10). In addition, Eq. (13d) specifies the initial condition of the problem, setting it to the current state estimate $\boldsymbol{x}_0$. The terminal condition Eq. (13e) guarantees the system comes back to the reference path by the end of the prediction horizon.

Within `AWEbox`, both the trajectory generation and path-tracking OCPs are formulated as non-linear programs (NLP) using the symbolic formalism from `CasADi` (Andersson et al., 2019). Then the interior-point NLP solver `IPOPT` (Wächter and Biegler, 2006) is used with the linear solver *MA57* (HSL). The discretization of the OCPs is achieved through direct collocation with Radau fourth-order polynomials. Additional implementation details are provided in De Schutter et al. (2023).

A two-way coupling is established between the flow solver, in which the aerodynamic forces and moments are computed, and the dynamics and control module. At each time step, the kite AL model evaluates the aerodynamic forces and moments given the current state vector $\boldsymbol{x}^n$ and the flow data. Those forces and moments are then transmitted to the dynamics and control module. Within the latter module, the NMPC controller updates the control inputs vector $\boldsymbol{u}$ at regular time intervals, based on the deviation from the reference trajectory. The updated control inputs are then used to compute the next state $\boldsymbol{x}^{n+1}$, given the 6-DOF AWES dynamics. The integration of the dynamics is performed using a fourth-order Runge-Kutta scheme. The next state is then sent to the flow solver, and the process starts over. Again, for the NMPC, the simplified analytical aerodynamic model described in Sect. 2.5.1 is used.

The coupling algorithm of the LES and AL kite model with the dynamics and NMPC flight path tracking is depicted in Fig. 4. The flow solver, the dynamics and the control have different characteristic time scales. During one flow time step Δt_{fluid}, once the forces and moments are evaluated, the dynamics is integrated with a time step Δt_{dyn}. The control is evaluated only when

https://doi.org/10.5194/wes-2025-288
Preprint. Discussion started: 9 January 2026

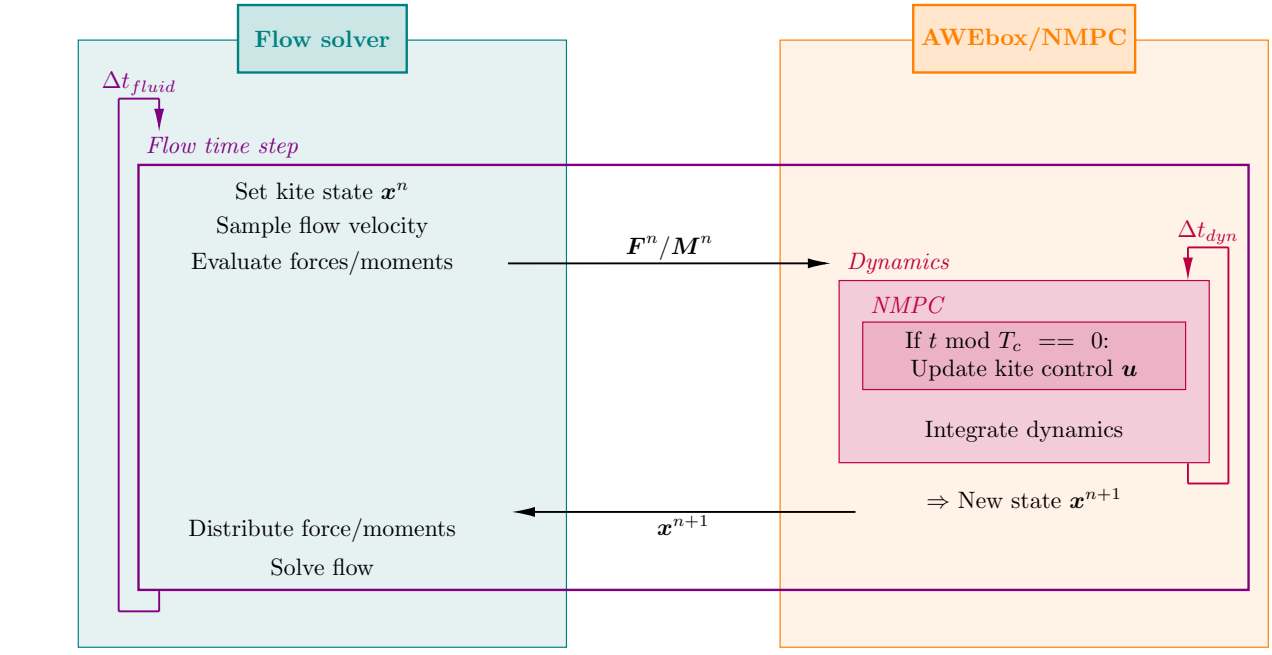

Figure 4. Schematic of the coupling of the flow solver and aircraft model with the dynamics and path tracking modules.

3 Accuracy verification

The wingspan of the kite drives the numerical discretization size of the problem. Here, the wingspan b is quite small compared to the trajectory that it flies, and hence many grid points are needed in the numerical flow domain. In a previous work (Crismer et al., 2024), the trajectory diameter D was about $5\,b$, and we used a domain with frontal area of $3\,D \times 3\,D$. The wingspan corresponded to about 17 grid points (when the AL is aligned with the grid) and the total domain contained about 50 million cells. In this work, the trajectory diameter is taken twice larger, so as to better reproduce realistic trajectories. This section thus aims at defining the discretization and domain size requirements in order for the simulation to be as accurate as possible while maintaining an affordable computational cost; as is required to be able to investigate multiple scenarios.

3.1 Wing discretisation

In this section, we investigate the requirements in terms of flow solver grid cell points and AL control points requirements to ensure a good representation of the wing aerodynamic properties. To this end, the aircraft, without its control surfaces, is considered in steady level flight at an angle of attack of $-5°$. The aircraft has a zero lift angle of $-11°$.

https://doi.org/10.5194/wes-2025-288
Preprint. Discussion started: 9 January 2026

eawe european academy of wind energy
Open Access WIND ENERGY SCIENCE DISCUSSIONS

The chosen number of grid points per wingspan sets the flow solver grid cell size. The the number of AL control points must be larger; yet it can be "only a bit larger" (i.e. about 1.2 times larger). This lower bound was determined such that the discretized AL takes full advantage of the grid resolution for the velocity sampling, but without overkill (i.e., in the sense that using more control points does not improve the results further), see Trigaux et al. (2024a). Concerning the mollification width σ of the Gaussian template, it is taken to be $2\,h$, where h is the flow solver grid size.

Figure 5 shows the distribution of the lift and drag coefficients for different numbers of grid points per wingspan. We have $\sigma = \bar{c}/4$ for the highest resolution and $1.5\,\bar{c}$ for the lowest one. One can note that the accuracy is still very good close to the tip for the lowest resolution. The main differences appear near the middle of the wing, where the lowest resolution leads to an overestimated lift and underestimated drag. The total lift slope coefficients are 0.604, 0.619, and 0.627 for 96, 32, and 16 points per wingspan, respectively. The total drag coefficients are 0.0237, 0.0234, and 0.0228, respectively. The difference between the finest and coarsest resolutions is $< 4\%$ for both lift and drag. This indicates that, despite the slight difference in loading in the middle of the wing, 16 grid points are enough to still have a fairly accurate representation of the wing aerodynamic loads. This also corresponds to the resolution used in (Crismer et al., 2024).

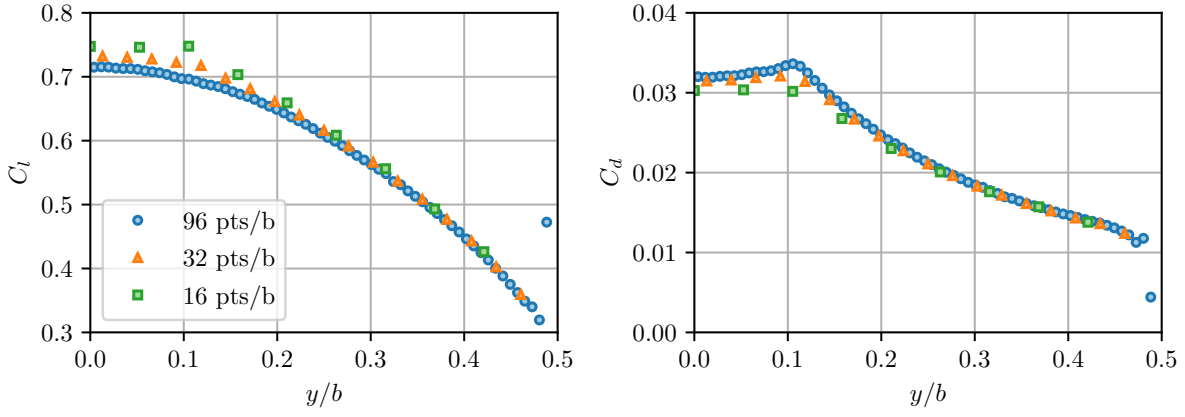

Figure 5. Comparison of the lift and drag coefficient distributions along the half span for different numbers of grid points per wingspan, and with 1.2 times more AL control points.

When varying the number of AL control points for a given number of grid points per wingspan, here 16, the wing loading hardly changes at all, as depicted in Fig. 6. The difference in terms of total lift and drag is of the order of a tenth of a percent. The accuracy is therefore conserved regardless of the number of control points, as long as it is larger than the number of grid points. In the following, 1.2 times the number of grid points will be used.

3.2 Domain size

To investigate the domain size, the single-loop trajectory from Crismer et al. (2024) is flown with MPC path tracking in domains of different sizes. The trajectory diameter D is about $5\,b$. The domain is $9\,D$ long and has a square frontal area of height H,

https://doi.org/10.5194/wes-2025-288
Preprint. Discussion started: 9 January 2026

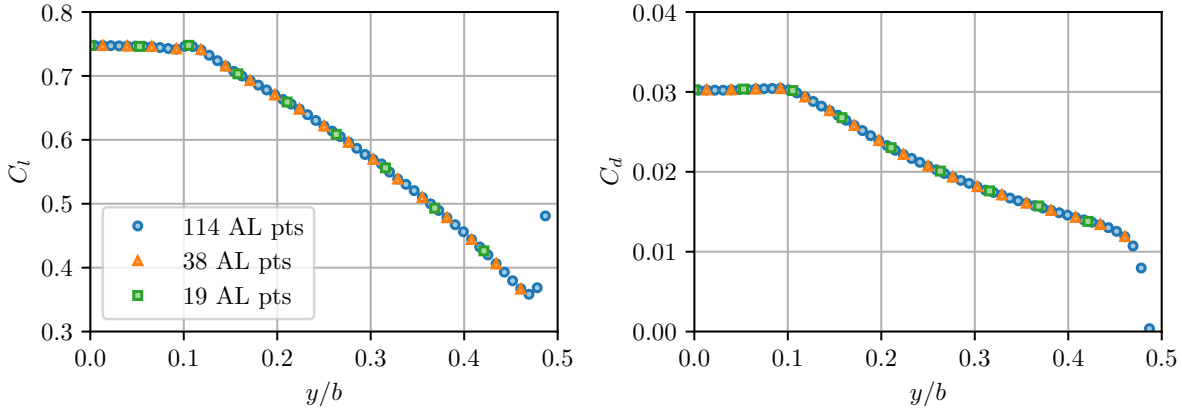

Figure 6. Comparison of the lift and drag coefficient distributions along the half span for different AL control points discretization, with 16 grid cell points per wingspan

.

with periodic conditions on the sides, and slip conditions on the top and bottom (ground location). The trajectory was flown, in domains with $H = 2\,D$, $3\,D$ and $6\,D$. Assuming a circular trajectory orthogonal to the mean wind, the swept area of the trajectory corresponds to 15.7 %, 7.0 %, and 1.7 % of the total frontal area, respectively. The mean power measured during 12 power cycles after the flow is developed is 770.8, 777.7 and 775.3 kW, respectively. The greatest difference is less than one percent, which indicates that a domain with $H = 2\,D$ is already enough for the flow to have negligible blockage effects. In this work, we consider larger trajectories for which the diameter is about $10\,b$. Since the ratio of the swept area to the frontal area scales with b/D, increasing D reduces the swept-area fraction for a given domain size expressed in terms of D.

4 Simulation setup

This section details the different simulation parameter choices. We first detail the trajectory generation and control in Section 4.1. The computational settings of the LES are given in Sect. 4.2.

4.1 Trajectory and control

The trajectory is a four-loop trajectory, generated using `AWEbox`. It is computed for a uniform inflow $U_\infty = 12\ \mathrm{m\,s^{-1}}$. It is depicted in Fig. 7. The resulting trajectory has a spatial footprint of 674 m $\times$494 m $\times$ 407 m. We define a characteristic length $D = 10\,b$, which approximately corresponds to the "characteristic diameter" of the trajectory, see Fig. 8. The kite rotates clockwise when looking downstream. The kite flight velocity ranges from 16.4 to 89.4 $\mathrm{m\,s^{-1}}$ over the whole trajectory, with an average value of 55.6 $\mathrm{m\,s^{-1}}$. The kite flies faster during the reel-out phase, with an average flight velocity of 67.8 $\mathrm{m\,s^{-1}}$, and reaches a minimum of 50.7 $\mathrm{m\,s^{-1}}$ at the end of the ascending parts of the loops. The velocity then decreases drastically during

https://doi.org/10.5194/wes-2025-288
Preprint. Discussion started: 9 January 2026

eawe european academy of wind energy
Open Access WIND ENERGY SCIENCE DISCUSSIONS

the reel-in phase. The trajectory has a time period $T_p = 112$ s and we define the dimensionless time t^* as t/T_p. A fraction of the fourth loop is used for starting the reel-in. The reel-out phase accounts for 70 % of the time and the reel-in phase for 30 %. The average power output is 1.38 MW and the instantaneous power can turn negative in the ascending phase of each loop to help the kite reach the top of the loop.

The set of constraints is applied to the state and control variables. They are provided in Appendix B, in Tables B1 and B2, along with the other constraints of the OCP and the NMPC. In addition to states and control variables, the instantaneous power is also limited to reduce the $P_{\max}/P_{\text{avg}}$ ratio. There are also constraints on aerodynamic quantities such as the angle of attack and the side-slip angle of the aircraft, and on the acceleration and tether force. The constraints are chosen to ensure operation within limits considered as acceptable for the different components of the system. They are tightened during the trajectory generation to have some additional freedom and margin during the flight path tracking.

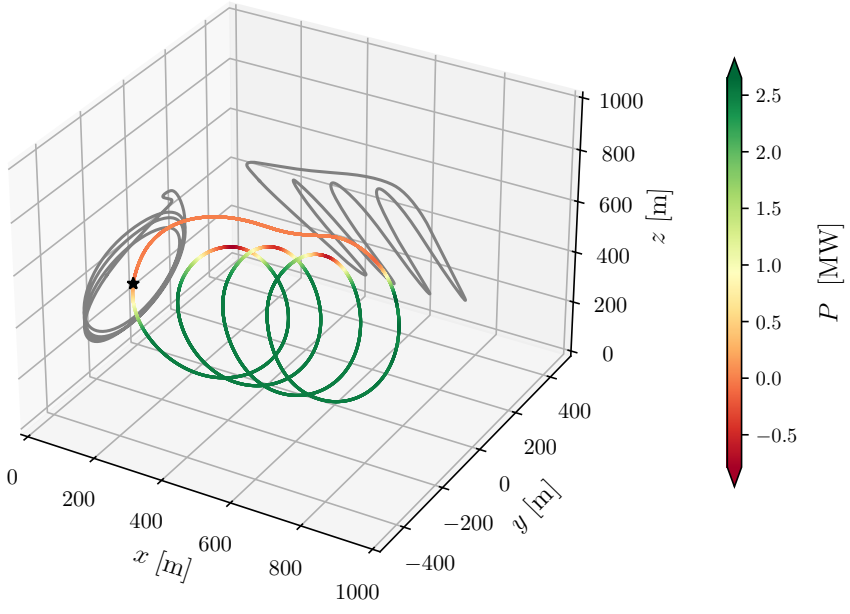

Figure 7. Four-loop trajectory generated using `AWEbox`, colored according to the instantaneous power output.

The kite controller is based on NMPC, as described in Sect. 2.5.2. The prediction horizon T_h of the NMPC corresponds to 20 NMPC sampling periods $T_c = 0.10$ s. During one sampling period the dynamics is integrated 20 times; each dynamics time step being 0.005 s.

https://doi.org/10.5194/wes-2025-288
Preprint. Discussion started: 9 January 2026

eawe european academy of wind energy
Open Access WIND ENERGY SCIENCE DISCUSSIONS

4.2 LES setup

The size of the domain is $5.4\,D \times 2.0\,D \times 1.36\,D$. This leads to a swept area corresponding to 11.5% of the domain frontal area which is shown to be sufficient in Sect. 3.2. The domain is discretized using $1024 \times 384 \times 256$ grid cells, which corresponds to a uniform spatial resolution of 2.25 m. This leads to 19 grid cells per wingspan. We use periodic conditions on the sides, and slip conditions on the top and bottom. The domain is shown in Fig. 8. The lower boundary of the domain corresponds to the ground, and the z-coordinate therefore denotes the altitude. The first kite trajectory is located so that it stays at least 3 wingspans away from the inlet. When there is also a second kite, it is placed as close as possible, ensuring that the tethers do not intercept (straight tethers). As the study focuses on the turbulent nature of the inflow and the kite's flight, we chose a uniform inflow of $12\ \mathrm{m\,s^{-1}}$ with an synthetic turbulence obtained using the Mann algorithm. The turbulence intensity is 6% and is representative of offshore ABL conditions. The precomputed box of turbulence has a spatial resolution of 4.5 m and is therefore linearly interpolated at the domain inlet. The box is long enough to last 6 power cycles. The time step used for the flow solver is 0.020 s. The investigations are carried out after the flow and the wake have developed during 2 power cycles (which corresponds to flowing 1.17 times the entire length of the domain), and during 6 additional power cycles.

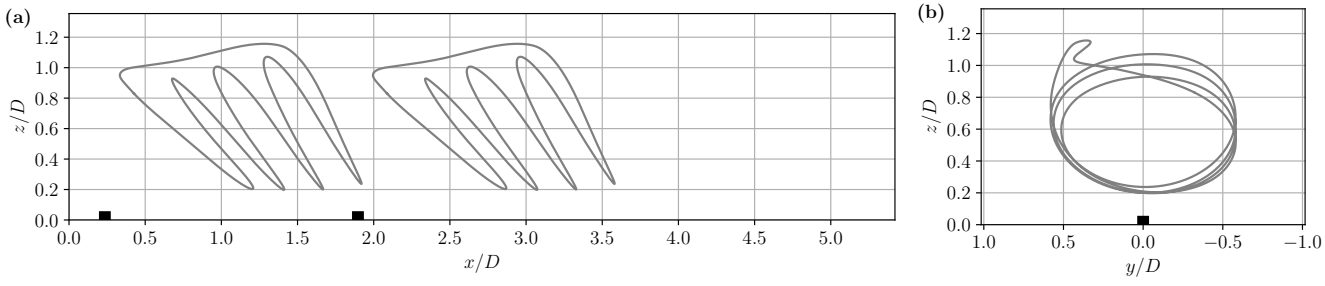

Figure 8. Illustration of the computational domain and flight region of the two kites, shown in side view (a) and front view (b). Black rectangles indicate the tether attachment points, corresponding to the ground-station locations.

5 Results and discussion

This section presents the results obtained for the various cases investigated. The first subsection is dedicated to the results obtained for a single kite. The next subsections detail the results for two kites, when the second one is placed behind the first one, and at different locations.

5.1 Single kite

When the kite flies alone, it is only subject to the inflow velocity wind and its turbulence. In the case of a uniform turbulent inflow with 6 % turbulence, the kite follows the trajectory without particular difficulty. The different quantities studied are represented as the average of what is performed by the kite during the six power cycles analyzed. A shaded area surrounds that

https://doi.org/10.5194/wes-2025-288
Preprint. Discussion started: 9 January 2026

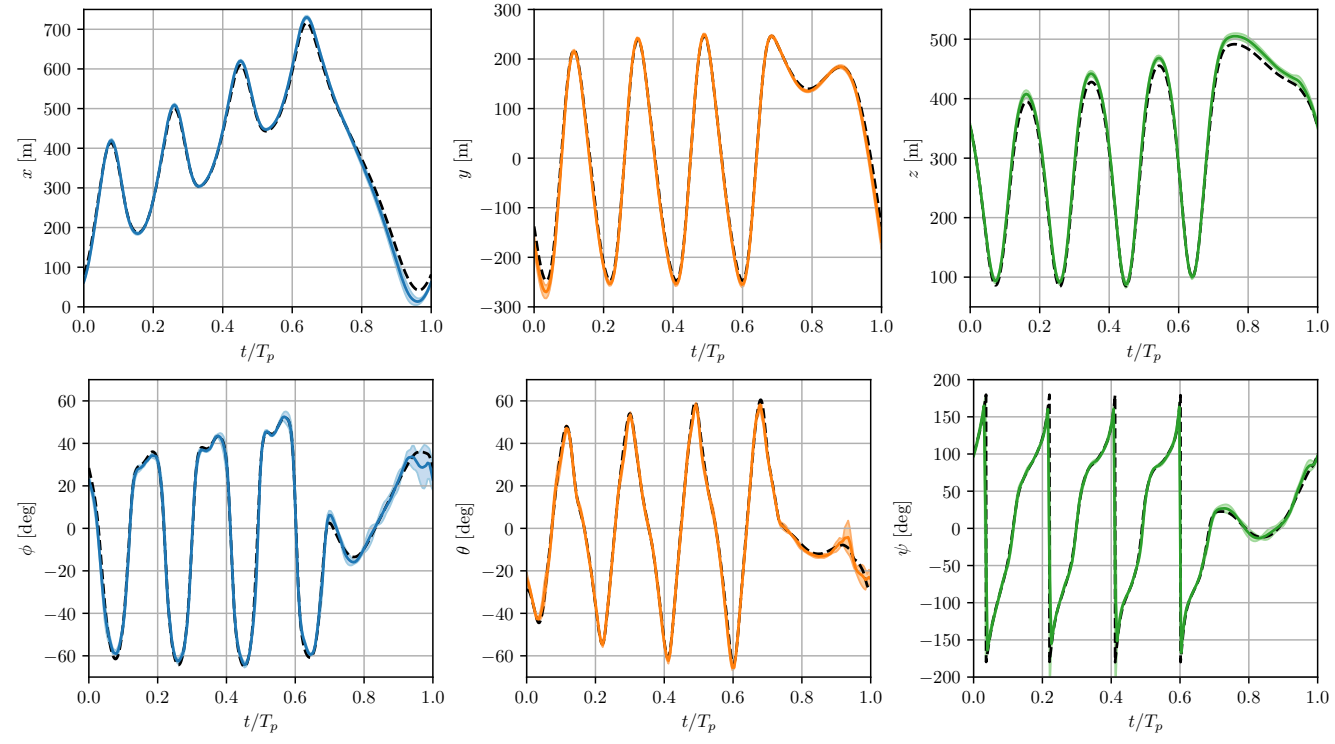

Figure 9. Six-cycle averages of the position and Euler angles, shown as solid colored lines with the corresponding standard deviation indicated by shaded areas, for LES with an AL model in a 6 % TI flow. The `AWEbox` reference is indicated by the dashed black line.

The actuation of the control surfaces is presented in Fig. 10. Although it remains close to the references, some deviations result from the controller mitigating the turbulence of the inflow. The average deflection of the ailerons remains fairly close to the reference, while it varies significantly from one cycle to another. The elevator actuation shows fast variations, yet up to max 6°, and the rudder is a bit less used at maximal positive deflection than planned. The reel-out phase, where the kite will roll and pitch to come back facing the wind, is well identifiable after $t/T_p = 0.7$.

The force and moment coefficients, in the body frame, are provided in Fig. 11. They are expressed in the body frame, as depicted in Fig. 2. The forces from the simulations are close to those from the reference. The vertical force coefficient C_z remains quite constant during the reel-out phase. Regarding the moments, the rolling and pitching moments are quite noisy. This likely indicates a larger mismatch between the simplified model and the AL-based model for these quantities. The yawing moment is more precisely reproduced. The moments show a high variability due to the encountered perturbations and the actuation of the control surfaces used to mitigate them.

https://doi.org/10.5194/wes-2025-288
Preprint. Discussion started: 9 January 2026

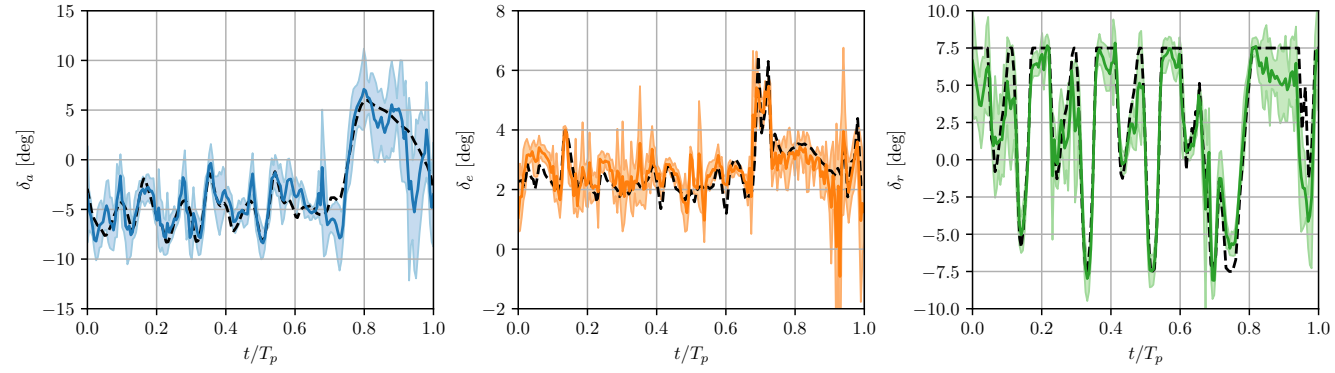

Figure 10. Six-cycle averages of the control surfaces deflection angle, shown as solid colored lines with the corresponding standard deviation indicated by shaded areas, for LES with an AL model in a 6 % TI flow. The `AWEbox` reference is indicated by the dashed black line.

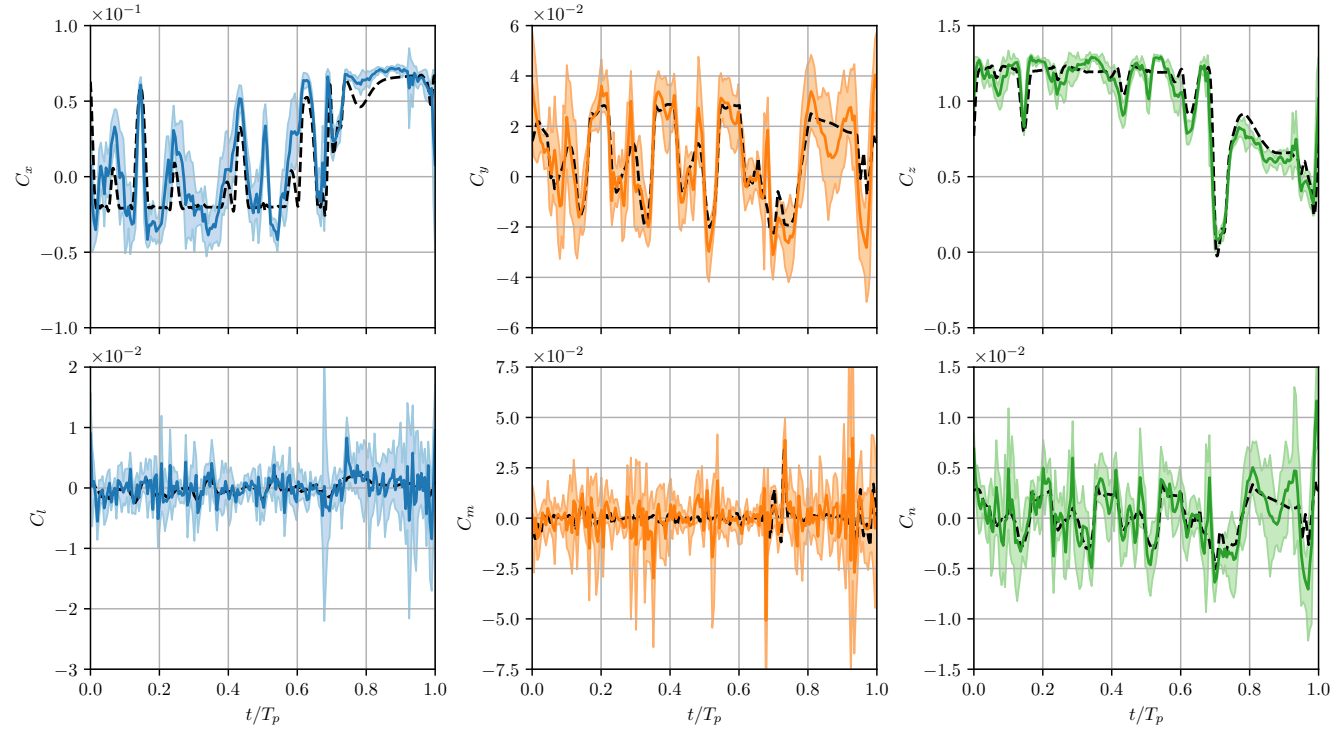

Figure 11. Six-cycle averages of the forces and moments expressed in the body frame, shown as solid colored lines with the corresponding standard deviation indicated by shaded areas, for LES with an AL model in a 6 % TI flow. The `AWEbox` reference is indicated by the dashed black line.

https://doi.org/10.5194/wes-2025-288
Preprint. Discussion started: 9 January 2026

eawe european academy of wind energy
Open Access WIND ENERGY SCIENCE DISCUSSIONS

The tether acceleration and traction, and the power output are very well followed, as seen in Fig. 12. The averaged cycles are close to the reference, and the inter-cycle variation is very low. One can see that the tether speed turns negative at the end of each loop. This is what makes the power negative and helps the kite go up at the end of the ascending phase of a loop, as pointed out in Sect. 4.1. The reel-in phase can be identified as the tether speed becomes highly negative at the end of the power cycle. The tether traction is always positive and it reaches maxima when the kite is at the bottom of the loop with maximum velocity. It is interesting to note that the tether traction is here null during the reel-in phase, corresponding to zero power consumption. The fact that it is zero is due to the simplified hypotheses of the `AWEbox` model (there is no model for the generator and the drum, and the tether is considered straight). During the reel-in phase, the kite essentially flies like a glider. It compensates for both its weight and that of the tether and is continuously descending; all of that without energy consumption. Here, the kite only consumes energy at the end of each loop, during the ascending phase.

One can also note that the tether traction, which is closely related to the vertical force on the kite, fluctuates a lot during the power cycle. Although the vertical force coefficient is more or less constant during the reel-out, the kite flight speed experiences large fluctuations, and so does the relative air velocity, resulting in large variations in vertical force magnitude. The averaged power is also close to the reference, despite some deviation during the first and fourth loops. The inter-cycle variation is quite low. The power production reaches a plateau during each loop due to the maximal power constraint. The total average power production is 1.39 MW, to be compared to the 1.38 MW planned by `AWEbox`. The RMS error on the mean power output of the 6 flown power cycles is 0.8% of the reference power output.

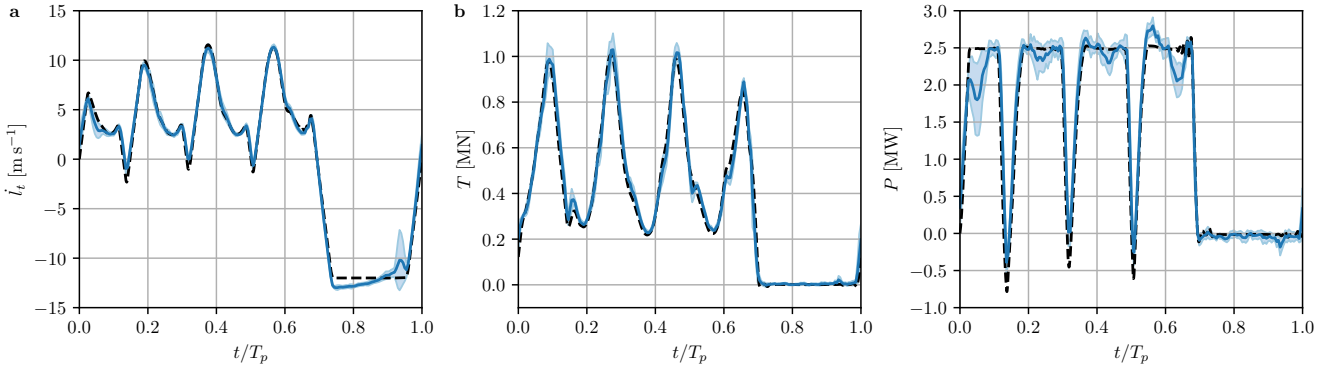

Figure 12. Six-cycle averages of the tether speed (a), tether traction (b), and power (c), shown as solid colored lines with the corresponding standard deviation indicated by shaded areas, for LES with an AL model in a 6 % TI flow. The `AWEbox` reference is indicated by the dashed black line.

The angle of attack and wing loading along the span are displayed in Fig. 13, where $\boldsymbol{f}_a$ stands for the aerodynamic force per unit length. Let us first note that the loading is almost symmetric during the reel-in phase because the kite comes back in a quasi-level flight towards its anchor point and with a reduced loading. However, it is slightly skewed towards the starboard side of the wing during the reel-out phase due to the rotation. In terms of force coefficient, the loading barely varies during the reel-out phase, as does the angle of attack. However, as already pointed out, it varies greatly in terms of magnitude due to the

https://doi.org/10.5194/wes-2025-288
Preprint. Discussion started: 9 January 2026

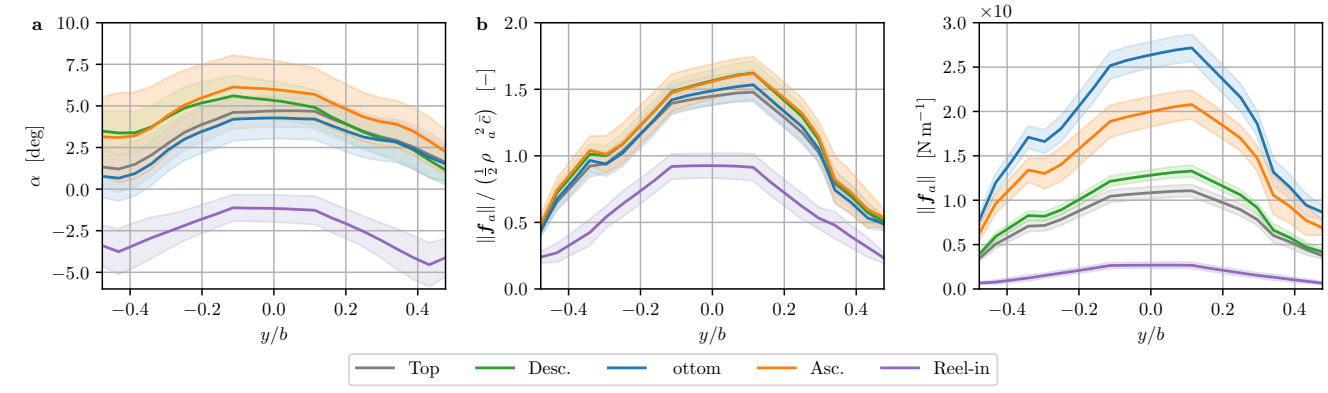

Figure 13. Six-cycle averaged aircraft angle of attack (a) and wing loading, dimensionless (b) and dimensional (c), together with their standard deviation (shaded area), for LES with AL in a 6 % TI flow. They are represented when the kite is at the top and bottom positions, and in the middle of the descending and ascending phases, of the reel-out loops, as well as during the reel-in phase

A vertical longitudinal cut and a vertical transversal cut $2D$ form the inlet of the mean streamwise velocity field are displayed in Fig. 14. Two elements can be outlined. First, the velocity deficit is located mainly at the bottom of the trajectory. Second, the magnitude of the normalized velocity deficit is fairly low and goes only up to $0.06U_\infty$. For comparison, the velocity deficit of wind turbines can be on the order of $0.3U_\infty$, even a few diameters downstream of the turbine, see for instance (Coquelet et al., 2022). The transversal cut shows that the velocity deficit is concentrated on the lower half of the loop, and slightly rotated clockwise. This corresponds to parts of the trajectories where the aerodynamic forces are larger, as seen in Fig. 15. A follower kite will therefore see a lower velocity in that area. The low averaged velocity deficit is due to the nature of the wake produced by such four-loops trajectory. Indeed, the loading of the kite is very low during the reel-in phase, which accounts for 30% of the trajectory time period, and the kite mainly produces a wake during the reel-out phase. The wake is therefore discontinuous in space and time, and released in batches, resulting in a low time-average velocity deficit.

Those discontinuities can be observed in Fig. 16, which shows an instantaneous field of streamwise velocity deficit. On the left, a longitudinal (a) cut shows the instantaneous velocity deficit just after the kite lowest position in its fourth loop. The passage of the kite left traces around $z \simeq 0.2\,D$ at $x \simeq 2.2$, 2.5, 2.8 and $3.1\,D$. Those traces have already decreased in intensity since the time they were released and are no longer stronger than the ambient turbulence. The maximum deviation from the inflow velocity in that cut is 33% and it will become even lower by the time it reaches the second kite flight area. However, in the vicinity of the kite, the induced velocity can be quite significant. The transversal cut is taken when the kite is near its maximal loading, at the bottom part of the second loop. The position and near wake of the kite is clearly identifiable, and the velocity deficit in that plane goes as low as 85% of U_∞ (out of the colormap range). It corresponds to the maximal velocity

https://doi.org/10.5194/wes-2025-288
Preprint. Discussion started: 9 January 2026

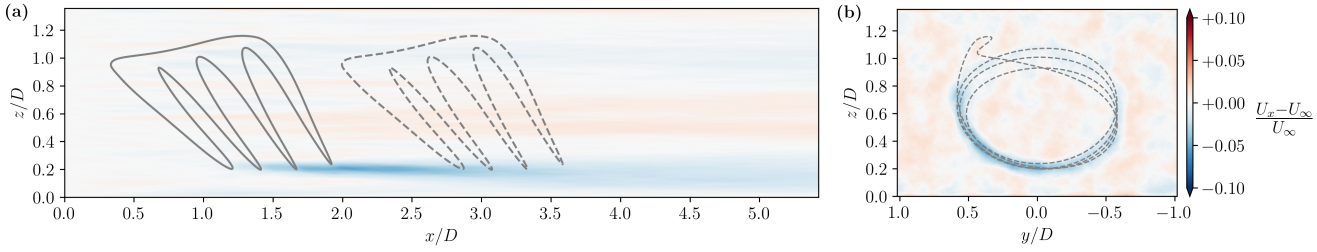

Figure 14. Six-cycle averaged streamwise velocity deficit of a single kite wake in a vertical longitudinal (a) and transversal plane at 2 D from the inlet (b). The location of a virtual kite downstream in indicated with dashed line.

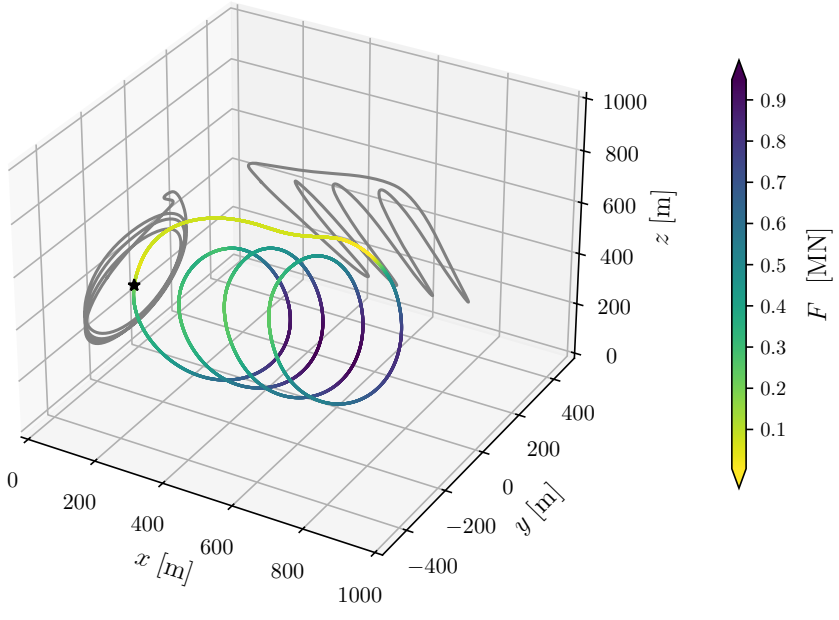

Figure 15. Four-loop trajectory generated using `AWEbox`, colored according to the aerodynamic force norm.

https://doi.org/10.5194/wes-2025-288
Preprint. Discussion started: 9 January 2026

eawe european academy of wind energy
Open Access WIND ENERGY SCIENCE DISCUSSIONS

induced by the tip vortices. This observation is consistent with the kite's flight velocity at this stage of its trajectory, which reaches $89.4\ \mathrm{m\,s^{-1}}$. Relative to its flight velocity the deficit is only of 11%. This is of the order of magnitude of the downwash that can be expected for such aircraft when flying at a high angle of attack.

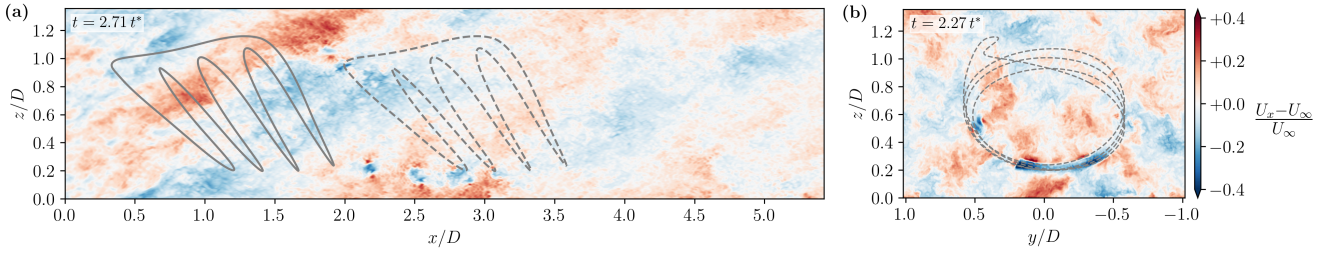

Figure 16. Instantaneous streamwise velocity deficit of a single kite wake in a vertical longitudinal (a) and transversal plane at $1.6\,D$ from the inlet (b).

5.2 Two kites in tandem

For the cases with two kites, both kites try to fly the same optimal reference trajectory. Two scenarios are investigated. For the first case, the second kite flies in-phase with the first kite. In the second case, the second kite trajectory is phase-shifted relative to the first kite's trajectory. In order to isolate the effect of the wake of the first kite, we perform additional simulations of the second kite only. Those simulations latter referred as "2$^{\mathrm{e}}$ only" will assess the effect of the ambient turbulence on kite 2.

5.2.1 In-phase flight

When the kites fly in-phase, the kites have, at every moment, the same reference state. In this specific scenario, the simulation shows that the second kite does not interact with the first kite's wake. This depends on the kite spacing, inflow velocity, and trajectory period.

Here, as illustrated in Fig. 17, the second kite reel-out occurs in almost unperturbed flow and it reels in while the first kite wake is passing by. Furthermore, as the kite reels in on the side, it also avoids the wake. Therefore, the first kite wake does not affect the second kite's power production phase.

This can be verified through simple calculations. The reasoning depicted in Fig. 18. In that figure, the parallelograms represent the wake of kites. The wake of the first kite is a structure released during its reel-out phase. At the end of this phase, at a time $t_{\mathrm{RO}} = n\,T_p + T_{\mathrm{RO}}$, the wake of the first kite extends downstream starting from the position of the first kite, $x_1(t_{\mathrm{RO}})$. At this time, both kites enter the reel-in phase, and the second kite reels in from $x_2(t_{\mathrm{RO}})$ to $x_2(t_p) \simeq (806 + 70)\,\mathrm{m} = 876\ \mathrm{m}$. The start of the trajectory, at a time $t_p = (n+1)\,T_p$, corresponds approximately to the end of the reel-in phase. During this time interval, the wake of the first kite is advected downstream. The relevant question is therefore: where is the wake of the first kite when the second kite starts its reel-out phase? The wake of the first kite is advected from $x_1(t_{\mathrm{RO}})$ over a duration of $T_p - T_{\mathrm{RO}} \simeq 41\ \mathrm{s}$ at an advection velocity U_{adv}. Here, the advection velocity of the wake is assumed to be close to the

https://doi.org/10.5194/wes-2025-288
Preprint. Discussion started: 9 January 2026

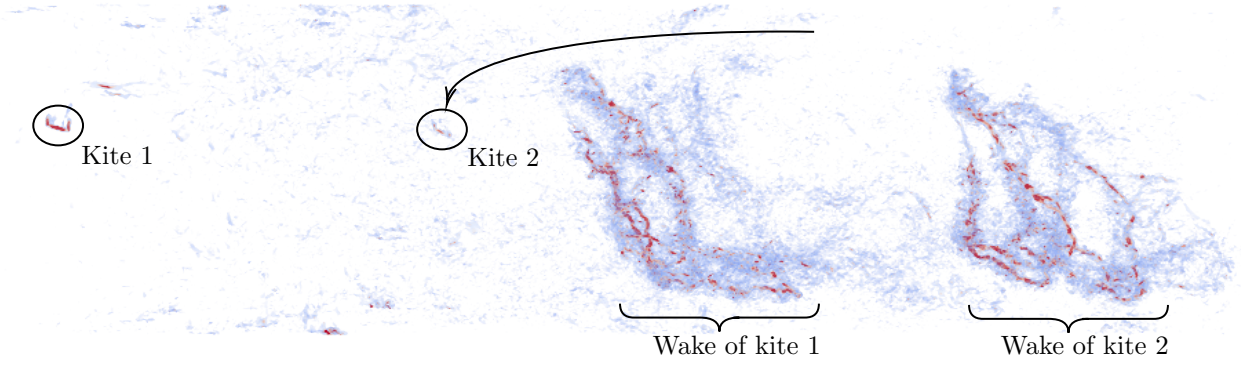

Figure 17. Instantaneous vorticity field volume rendering, at the beginning of a reel out phase, for a two-kite configuration where the kites fly in-phase; illustrating the second kite avoiding the first kite's wake.

mean velocity within the wake and is estimated to be approximately $11\ \mathrm{m\,s^{-1}}$ (see Fig. 14). The wake is therefore located at $x_1(t_{\mathrm{RO}}) + U_{\mathrm{adv}}(T_p - T_{\mathrm{RO}}) \simeq \big((100+715)+11\times 41\big)\,\mathrm{m} = 1266\ \mathrm{m}$. When the second kite resumes its trajectory, the wake of the first kite is already far downstream.

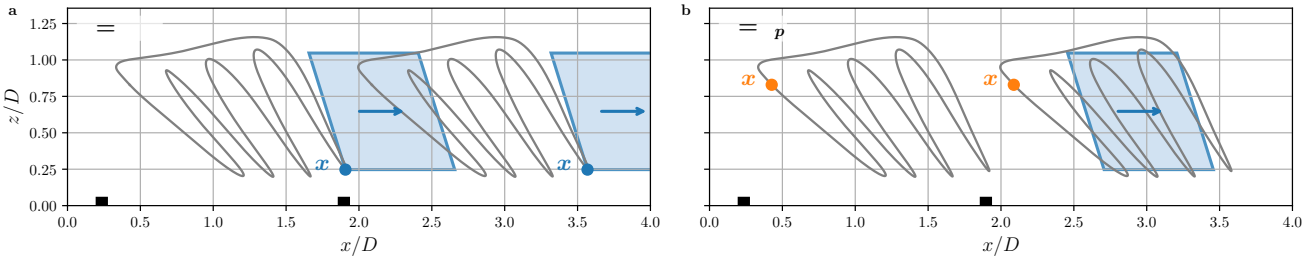

Figure 18. Schematic illustrating the wake interaction for a two-kite configuration with in-phase trajectories.

The second kite experiences almost no additional perturbation other than ambient turbulence and operates as efficiently as the first kite. The mean power is 1.39 MW for the first kite and 1.40 MW for the second kite. Figure 19 shows the error with respect to the reference. It is evaluated by taking the RMS of the vector norm of the difference between the results and the reference, i.e. $\epsilon(\boldsymbol{q}) = RMS(\|\boldsymbol{q} - \boldsymbol{q}_{\mathrm{ref}}\|)$. In terms of position, the RMS error compared to the reference is limited to $1.1\,b$. For the forces, it goes up to 20% of the force range but is most of the time below 10%. It is also very close to the case without the first kite, confirming that the first kite has almost no influence on the operation.

The first and second kites' average power production cycles are very similar, as depicted in Fig. 20. Their mean power is 1.39 and 1.40 MW, respectively. The power output of the second kite is identical when the first kite is removed.

The average velocity deficit shown in Fig. 14 could suggest that the second kite has been exposed to lower velocities. However, as the four-loop trajectory is not continuous in its wake shedding, considering averaged flow quantities is not consistent

https://doi.org/10.5194/wes-2025-288
Preprint. Discussion started: 9 January 2026

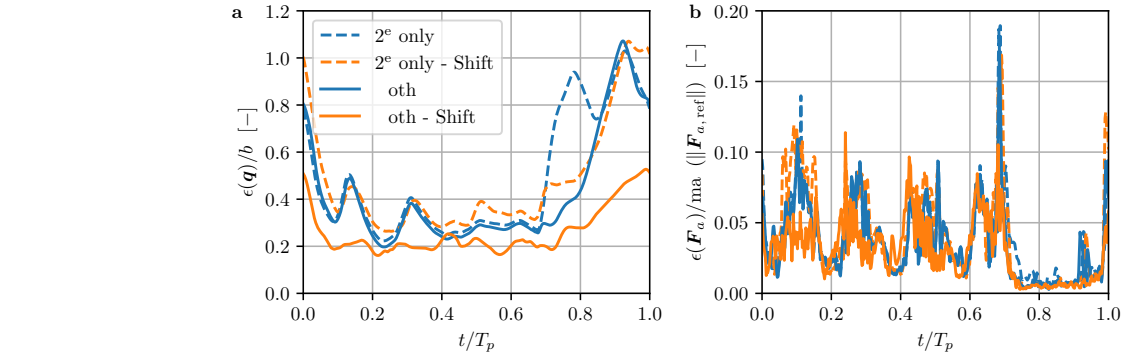

Figure 19. Six-cycle averaged error in position (a) and forces (b) for the second kite flying in LES with AL in a 6 % TI flow, the in-phase or phase-shifted trajectory. It is compared to a "single" kite flying at the same place and with the same time delay (i.e., removing the first kite).

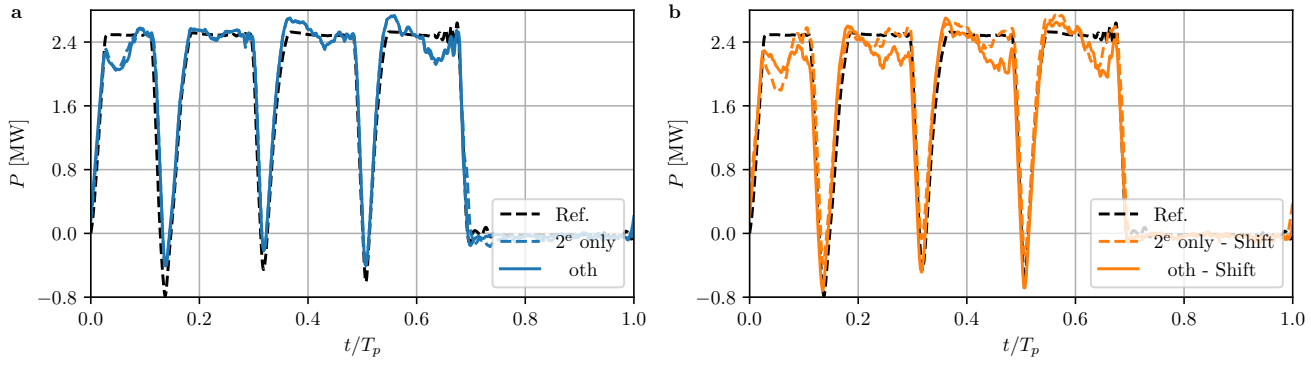

Figure 20. Six-cycle averaged power of the second kite flying in LES with AL in a 6 % TI flow the in-phase (a) or phase-shifted (b) trajectory; also compared to a "single" kite.

for drawing conclusions about follower performance, as the second kite can avoid the wake. The averaged velocity deficit of the kite tandem is shown in Fig. 23. The deficit is further increased by the second kite, from $0.05\,U_\infty$ to $0.08\,U_\infty$ and enlarged.

5.2.2 Phase-shifted flight

In this case, the second kite trajectory is phase-shifted so that the second kite flies in the wake of the first kite during its reel-out phase, as shown in Fig. 21.

The trajectory of the second kite starts at $0.43\,t^*$, instead of 0. This phase shift is evaluated as follows. The second kite must start its trajectory once the wake of the first kite has advected over the distance separating the two kite trajectories, equal to the distance between the ground stations L_s. This is illustrated in Fig. 22. The required delay is $T_s = \frac{L_s}{U_{\mathrm{adv}}} = 64.2$ s. The

https://doi.org/10.5194/wes-2025-288
Preprint. Discussion started: 9 January 2026

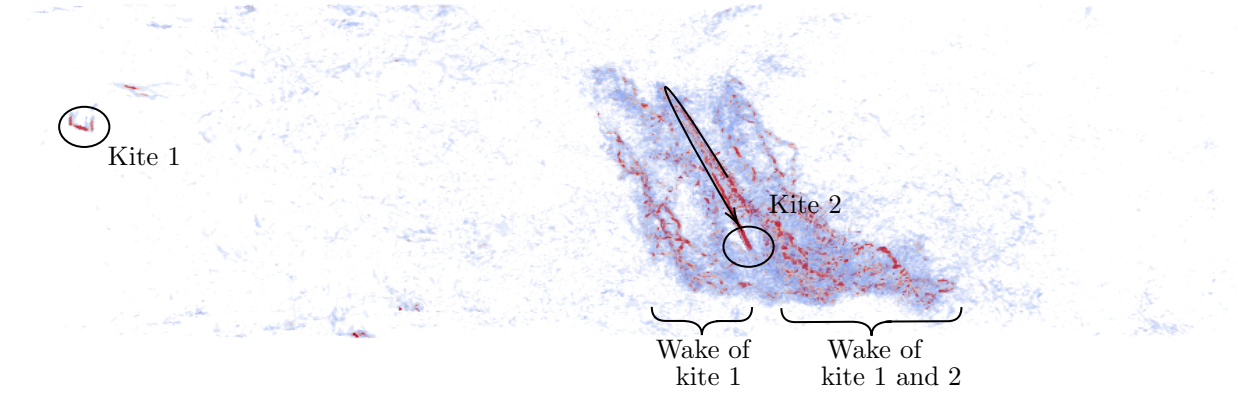

Figure 21. Instantaneous vorticity field volume rendering, at the beginning of a reel out phase of the first kite, for a two-kite configuration where the kites fly out of phase; illustrating the second kite flying in the first kite's wake.

second kite will start its trajectory at $t_s = nT_p + T_s$. Accordingly, the second kite starts the simulation at $T_p - T_s = 47.8$ s, corresponding to $0.43t^*$.

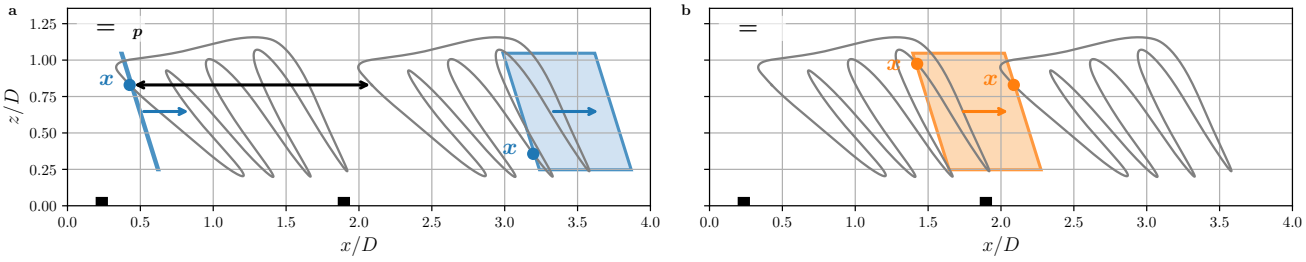

Figure 22. Schematic illustrating the wake interaction for a two-kite configuration with phase-shifted trajectories.

Again, the first kite experiences the same conditions than when it is alone and in the "in-phase" scenario. The second kite also flies well, despite the perturbation it encounters, as evidenced by the "Shift" curves in Fig. 19. The first kite's wake does not seem more harmful than the ambient turbulence already present in the inflow. Indeed, the kite flies quite fast, and perturbations must be large enough compared to its velocity to become significant. For example, the turbulence intensity is evaluated with respect to U_∞ which is 6 times lower than the mean kite speed during its reel-out phase. It is therefore much less significant for the kite, and this could explain why the kites are only weakly perturbed. Nevertheless, the power production of the second kite is affected by the velocity deficit induced by the wake of the first kite. It can be observed in Fig. 20 that the power output is lower during fractions of the loops. It should be noted that it only happens at specific times. During the reel-out phase, the kites move downstream at a lower velocity than the inflow. As a result, the length of the wake packet is shorter than the streamwise extent of the reel-out portion of the trajectory. Consequently, the wake of the first kite can only affect the follower during a

https://doi.org/10.5194/wes-2025-288
Preprint. Discussion started: 9 January 2026

eawe european academy of wind energy
Open Access WIND ENERGY SCIENCE DISCUSSIONS

fraction of its reel-out phase. In this case, the kites produce 1.38 and 1.30 MW, respectively. The second kite thus produces roughly 6 % less than the first one.

The trajectory shift of the second kite also affects the wake. This is evidenced in Fig. 23 (c) and (d), which displays the difference in velocity ΔU between the phase-shifted and the in-phase cases. It shows that the velocity deficit for the phase-shifted case is weaker in the upper parts of the loops, around $z/D = 1$ in Fig. 23(c). However, the deficit is further increased in the lower parts of the loops and broadened around $z/D = 0.2$.

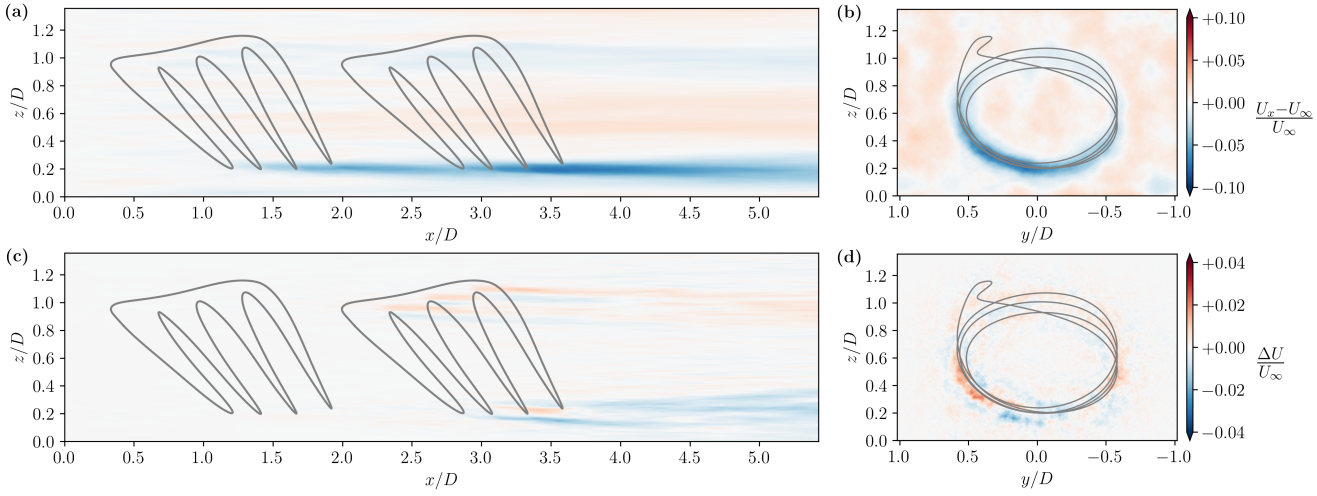

Figure 23. Six-cycle averaged streamwise velocity deficit of kites in tandem, where the second kite flies in-phase, in a vertical longitudinal (a) and transversal plane at $4\,D$ from the inlet (b); and difference in velocity ΔU caused by the trajectory phase shift on the second kite (c,d).

6 Conclusions

This paper presents a Large Eddy Simulation framework to perform simulations of ground-gen rigid-wing Airborne Wind Energy Systems. The framework is based on an LES flow solver developed in-house. Kites are represented by a model based on an Actuator Line for the main wing, complemented by models for the control surfaces (elevator, rudders, ailerons). In this framework, kites fly optimal trajectories as computed using `AWEbox` by solving optimal control problems. The flow solver is also coupled to the flight path tracking module of `AWEbox` to handle the control of the different kites in the simulation environment, using Model Predictive Control.

The framework is employed to investigate both a single kite operating in a turbulent flow and a pair of kites, the second one flying behind the first one. In the single kite case, we highlight the capability of the kite to fly its trajectory despite the 6 % turbulence intensity. The MPC controller performs well in handling the encountered turbulence and perturbations. The different control states are followed accurately during flight path tracking. The position and attitude remain very close to the reference, while some variability is observed in the actuation of the control surfaces and in the forces and moments. The yawing

https://doi.org/10.5194/wes-2025-288
Preprint. Discussion started: 9 January 2026

moment is well reproduced, while the rolling and pitching moments experience more variations. The precision of the simplified aerodynamic model could likely be improved regarding those aspects. The wing loading is shown to vary quite significantly during the trajectory and is also skewed because of the rotation, but its shape does not vary much. The average velocity deficit from the kite wake is weak. However, such trajectories produce discontinuous wakes in both space and time, so that the wake mostly induces local perturbations, which are not well characterized by the time-averaged velocity deficit.

In the first configuration considered of kites in tandem, the second kite is not perturbed at all by the wake of the first kite. It is in a configuration where it reels in while the first kite wake passes by, and it completely avoids it. The tracking is therefore also accurate. In a second scenario, the second kite is forced to fly in the wake of the first kite; which is done by introducing a phase shift in the start of its trajectory. Concerning the trajectory tracking, the encountered wake perturbations do not affect the second kite significantly, and it is able to correctly track its trajectory. Nevertheless, there is an impact on the power production, of about -6 %, due to the velocity deficit of the wake. We conclude that both the 6 % TI of the turbulent wind and the wake of the first kite are too small perturbations relative to the kite flight velocity to affect it significantly.

The investigations demonstrated the capability of the developed framework to perform simulations of kites in turbulent environments. We highlight the fact that kite wakes are intrinsically dependent on the kite trajectory and flight velocity and that, for the case of four-loop trajectories, the wake consists of discrete, identifiable perturbations that can eventually interact strongly and merge, yet that remain of a limited longitudinal extent. This suggests that wake avoidance strategies and sophisticated control schemes could be developed to minimize the net power losses due to wakes for multiple kite configurations. In follow-up work, we aim at investigating kites flying in/through other kinds of strong perturbations, such as a kite also crossing the wake of a large conventional wind turbine during its trajectory.

Code availability. The LES flow solver is a proprietary software of UCLouvain while the toolbox `AWEbox` is openly accessible on *GitHub* (https://github.com/awebox, AWEbox, 2025).

Appendix A: Kite geometry

Based on the MegAWES kite description in (Eijkelhof and Schmehl, 2022), the geometry of the kite considered in this work is further detailed. Some dimensions are adapted from Eijkelhof and Schmehl (2022). For example, the location and dimensions of the ailerons are corrected to coincide with the structural model obtained from the author. A detailed sketch of the adapted geometry is shown in Fig. A1.

The kite has a wingspan of 42.5 m and an aspect ratio of 12. The dash-dotted lines, in Fig. A1, represent the control surface hinges. They coincide with the quarter chord for the elevator and the rudders. The widely-spaced dashed line is the main wing quarter chord line. Note that the aileron gaps were created solely to facilitate mesh overset in the wing-resolved CFD of Pynaert et al. (2024), with whom we collaborate and are considered as part of the wing when using the AL. A detailed description of the wing planform is provided in Table 4 of Eijkelhof and Schmehl (2022). However, within the BORNE project, the wing

https://doi.org/10.5194/wes-2025-288
Preprint. Discussion started: 9 January 2026

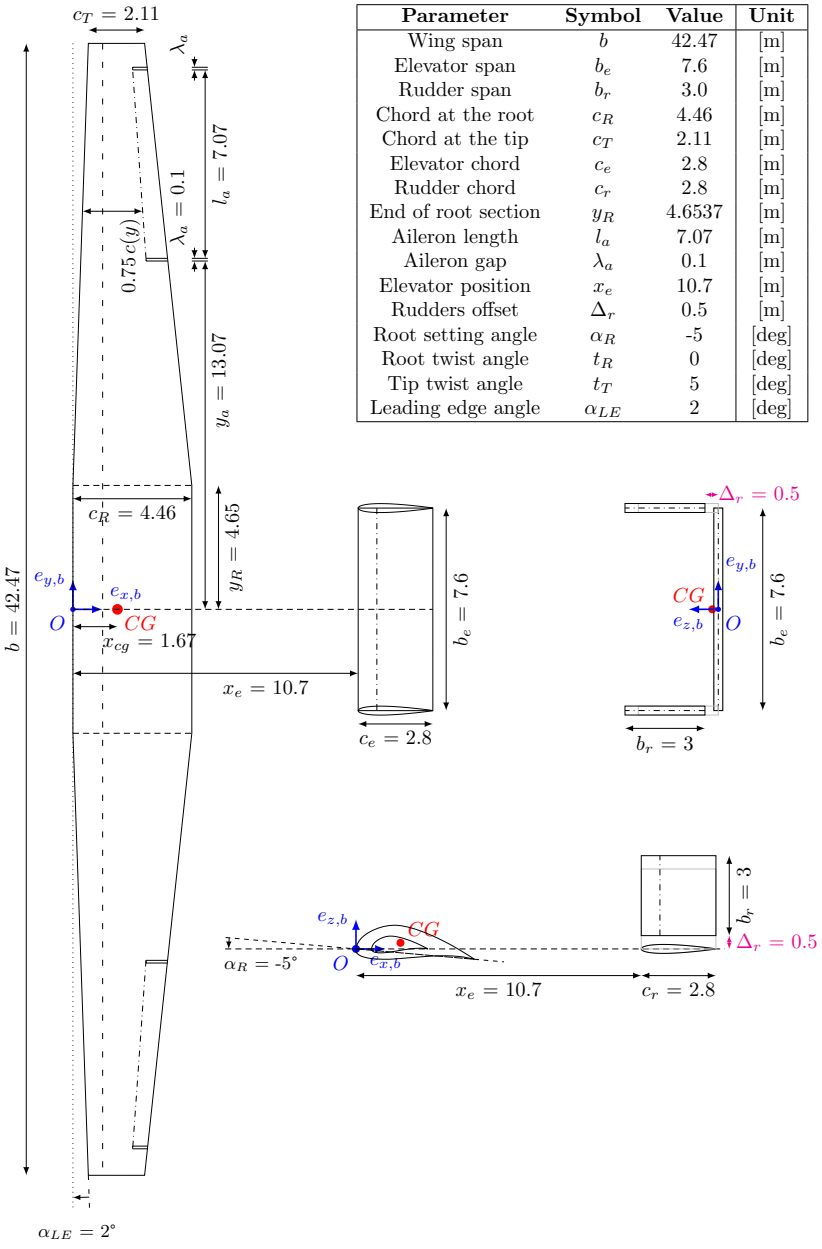

Parameter	Symbol	Value	Unit
Wing span	b	42.47	[m]
Elevator span	b_e	7.6	[m]
Rudder span	b_r	3.0	[m]
Chord at the root	c_R	4.46	[m]
Chord at the tip	c_T	2.11	[m]
Elevator chord	c_e	2.8	[m]
Rudder chord	c_r	2.8	[m]
End of root section	y_R	4.6537	[m]
Aileron length	l_a	7.07	[m]
Aileron gap	λ_a	0.1	[m]
Elevator position	x_e	10.7	[m]
Rudders offset	Δ_r	0.5	[m]
Root setting angle	α_R	-5	[deg]
Root twist angle	t_R	0	[deg]
Tip twist angle	t_T	5	[deg]
Leading edge angle	α_{LE}	2	[deg]

Figure A1. Top, port and back view of the MegAWES aircraft with its main dimensions.

https://doi.org/10.5194/wes-2025-288
Preprint. Discussion started: 9 January 2026

eawe european academy of wind energy
Open Access WIND ENERGY SCIENCE DISCUSSIONS

planform is slightly changed so that the final chord length and twist coincide with the data from Table 3 of the same reference. Here, we decide to assume linear chord and twist distributions.

The main wing chord is constant on the so-called root section, spanning from $-y_R$ to $+y_R$. Then it linearly decreases up to the tip from a chord length c_R to c_T. The point where the chord goes from constant to linear is chosen so that the planform surface keeps its area $S = 150.45$ m^2. The wing section is the $\mathrm{RevE_{HC}}$ aerodynamic profile (Eijkelhof, 2019). The two rudders and the elevator use a NACA0012 airfoil. The main wing is set at an angle of $-5°$ with respect to the aircraft x_0 axis and is linearly twisted from the end of the root section to the tip, where it reaches $t_T = 5°$ twist angle. The constant section is chosen to be the same as for the chord. The chord of the tip aerodynamic profiles have therefore aligned ($0°$ angle) with respect to the aircraft x_0 axis. The angles of the wing sections are defined as positive for washout and negative for washin. The chord and twist distribution are therefore respectively:

$$c(y) = \begin{cases} c_R & \text{if } y \leq y_R \text{ ;} \\ c_R + \frac{c_T - c_R}{y_T - y_R}(y - y_R) & \text{else.} \end{cases} \tag{A1}$$

$$t(y) = \begin{cases} t_R & \text{if } y \leq y_R \text{ ;} \\ t_R + \frac{t_T - t_R}{y_T - y_R}(y - y_R) & \text{else.} \end{cases} \tag{A2}$$

The value of y_R that maintains the right planform surface area is 4.65 m. The comparison between the reconstructed geometry and the data from Table 4 is shown in Fig. A2.

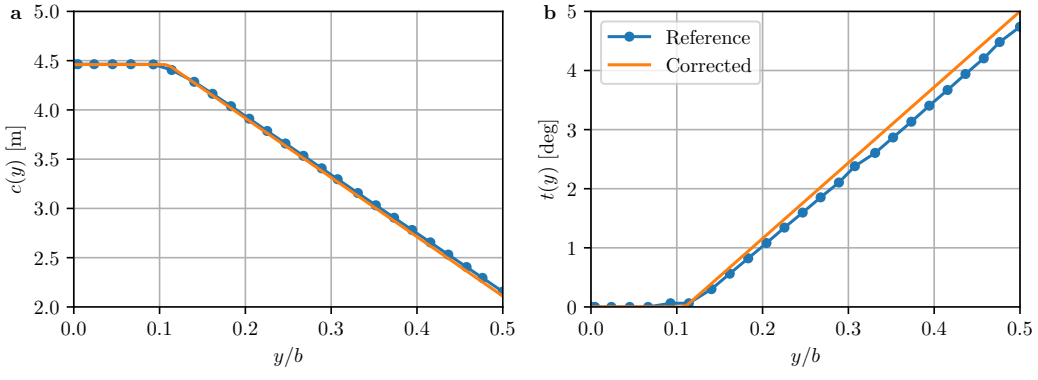

Figure A2. Comparison between the assumed chord (a) and twist (b) distribution data from Table 4 in Eijkelhof (2019).

Furthermore, we also assume that the quarter-chord line is straight, as the relative error on the x distance to the front of the wing-root is only 1.25%. Also, the coordinates of the center of gravity in the x forward, y to port, and z downward reference frame are $(-1.6729,\ 0.0,\ -0.2294)$. After discussion with the authors (Eijkelhof and Schmehl, 2022), it turns out that there was a typo in the z-coordinate sign in the original publication.

https://doi.org/10.5194/wes-2025-288
Preprint. Discussion started: 9 January 2026

eawe european academy of wind energy
Open Access WIND ENERGY SCIENCE DISCUSSIONS

Appendix B: Trajectory parameters

This Appendix gives the parameters used to generate the trajectory using `AWEbox`. The constraints on the states are given in Table B1, and the constraints on the control variables are provided in Table B2, along with some additional constraints, notably on important aerodynamic quantities. The OCP time horizon has been subdivided into 160 intervals (40 per loop). An additional parameter constraining the lower bound of the tether velocity during the reel-out phase is set to $-3.0\,\mathrm{m\,s^{-1}}$.

Table B1. Bound constraints applied to state variable $\boldsymbol{x}$ used in the optimal control problem. The maximal lateral extent of the flight path and the maximal tether length are respectively set to $y_{\max} = 225$ m and $l_{\max} = 1000$ m to limit the spatial footprint of the trajectories.

	Quantity	q_x	q_y	q_z	ω_x	ω_y	ω_z	δ_a	$\delta_{e,r}$	l	$\dot{l}$
	Units	[m]	[m]	[m]	$[\mathrm{deg\,s^{-1}}]$	$[\mathrm{deg\,s^{-1}}]$	$[\mathrm{deg\,s^{-1}}]$	[deg]	[deg]	[m]	$[\mathrm{m\,s^{-1}}]$
Generation	Min.	0.0	$-(y_{\max}+0.5b)$	$2b$	-10.0	-40.0	-25.0	-15.0	-7.5	0.0	-12.0
	Max.	l_{max}	$+(y_{\max}-0.5b)$	$+\infty$	$+10.0$	$+40.0$	$+25.0$	$+15.0$	$+7.5$	l_{max}	$+12.0$
Tracking	Min.	0.0	$-\infty$	$2b$	-50.0	-50.0	-50.0	-20.0	-10.0	0.0	-15.0
	Max.	l_{max}	$+\infty$	$+\infty$	$+50.0$	$+50.0$	$+50.0$	$+20.0$	$+10.0$	l_{max}	$+15.0$

Table B2. Bound constraints applied to control variable $\boldsymbol{u}$ and other variables used in the optimal control problem. The maximum tether tension is chosen as $T_{T,\max} = 1.7$MN as specified in Eijkelhof and Schmehl (2022).

	Quantity	$\dot{\boldsymbol{\delta}}$	$\ddot{l}$	T_T	$\ddot{\boldsymbol{q}}$	$\boldsymbol{v}_a$	α	β	$P_{\max}$
	Units	$[\mathrm{deg\,s^{-1}}]$	$[\mathrm{m\,s^{-2}}]$	[kN]	[g]	$[\mathrm{m\,s^{-1}}]$	[deg]	[deg]	[MW]
Generation	Min.	-25.0	-2.5	0.0	-3.0	10	-12.0	-5.0	-2.5
	Max.	$+25.0$	$+2.5$	$T_{T,\max}$	$+3.0$	120	$+4.0$	$+5.0$	$+2.5$
Tracking	Min.	-50.0	-5.0	0.0	-4.0	10	-15.0	-10.0	-3.0
	Max.	$+50.0$	$+5.0$	$T_{T,\max}$	$+4.0$	120	$+5.0$	$+10.0$	$+3.0$

https://doi.org/10.5194/wes-2025-288
Preprint. Discussion started: 9 January 2026

eawe european academy of wind energy
Open Access WIND ENERGY SCIENCE DISCUSSIONS

Appendix C: Stability derivatives

In the aerodynamic model described in (Malz et al., 2019), the force coefficients are expressed as a superposition of different contributions from the angle of attack, side-slip angle, kite angular velocities, and control surfaces actuations, as described in Eq. 11, 12a, and 12b. The sub-coefficients are evaluated for our AL-based model by imposing several movements to the kite in a simulations. The forces and moments are measured, and the sub-coefficients are obtained by inverting the model's equations. Such sub-coefficients are in fact second-order functions of the angle of attack α.

The LES framework allows one to impose the kite trajectory. A trajectory containing lateral motion, rotations in the three body axis direction, and the actuation of the three sets of control surfaces, at different angles of attack, is constructed. Once all the different movements are performed, the angle of attack is increased. The different movements do not require the kite to actually move in the flow domain, but the velocities induced by the movements considered are taken into account by the AL method.

The simulation is performed in a domain of $6b \times 4b \times 4b$ and the aircraft is facing a uniform inflow of $100\ \mathrm{m\,s^{-1}}$, which is of the order of magnitude of the velocity at which the kite operates. The kite is thus placed $1.5\,b$ behind the inlet in the center of the domain and stays at that position for the whole simulation. Each movement is applied to the kite during $1\mathrm{s}$, which corresponds to a flow displacement of about $2.5\,b$. Forces and moments are measured and averaged during the last $0.5\mathrm{s}$, where the measurements are converged and steady. The forces and moments measured at a certain angle of attack, without any other actuations or movements, are then subtracted from the measurements taken during the different motions or actuations to evaluate the ad hoc coefficients. The magnitude of the movements and actuations are provided in Table C1. They are chosen such that they represent either the mean or the most encountered value along the trajectory.

Table C1. Actuation magnitude used to evaluate the aerodynamic model coefficients.

Quantity	β	ω_x	ω_y	ω_z	δ_a	δ_e	δ_r
Units	[deg]	[deg s^{-1}]	[deg s^{-1}]	[deg s^{-1}]	[deg]	[deg]	[deg]
Actuation	2.0	0.05	0.05	0.25	7.0	3.0	8.0

The resulting coefficients are given in Table C2. It is to be noted that only the relevant terms are considered for each coefficient.

https://doi.org/10.5194/wes-2025-288
Preprint. Discussion started: 9 January 2026

eawe european academy of wind energy
Open Access WIND ENERGY SCIENCE DISCUSSIONS

Table C2. Aerodynamic coefficients of the MegAWES aircraft as evaluated using the AL. The coefficients represents a second order polynomial depending on α.

Coeff.	Term	a_0	a_1	a_2
C_X	0	-0.0406	+0.6091	+3.8723
	q	-0.5377	+2.5229	+5.8942
	δ_e	-0.0344	+0.3549	+0.2622
C_Y	β	-0.1763	-0.0019	+0.0955
	p	-0.0005	-0.0833	-0.3620
	r	+0.0744	-0.0089	-0.0368
	δ_a	+0.0014	-0.0066	-0.0166
	δ_r	+0.1762	+0.0047	-0.1778
C_Z	0	-0.9770	-4.0720	+6.2705
	q	-1.8502	-4.0302	-15.9874
	δ_e	-0.4516	+0.0922	+0.7698
C_l	β	-0.0074	+0.0009	+0.0153
	p	-0.5379	+1.6808	+8.1936
	r	+0.2211	+0.6395	+0.4973
	δ_a	-0.2415	-0.0879	-0.2742
	δ_r	+0.0073	+0.0000	-0.0050
C_m	0	+0.0618	-0.2795	-1.6016
	q	-6.7754	+0.4106	+3.1022
	δ_e	-1.2166	+0.0559	+0.9132
C_n	β	+0.0400	+0.0010	-0.0132
	p	-0.0830	-0.7384	+1.5599
	r	-0.0290	+0.0613	+0.0458
	δ_a	+0.0073	-0.1983	-0.0687
	δ_r	-0.0402	-0.0013	+0.0378

https://doi.org/10.5194/wes-2025-288
Preprint. Discussion started: 9 January 2026

eawe european academy of wind energy
Open Access WIND ENERGY SCIENCE DISCUSSIONS

Author contributions. JBC performed implementations in the LES flow solver and carried out the simulations. JBC analyzed the data with the insight of TH, MD and GW. JBC wrote the manuscript. TH, MD and GW revised the manuscript. The PhD work of JBC is supervised and advised by GW and MD.

Competing interests. The authors declare no competing interests.

Acknowledgements. This work is carried out as part of the BORNE project on "Developing the tools and insight to expand the Belgian offshore wind farms with airborne wind energy systems", funded by the Energy Transition Funds from the SPF Economy.

The present research benefited from computational resources made available on Lucia, the Tier-1 supercomputer of the Walloon Region, infrastructure funded by the Walloon Region under the grant agreement n°1910247.

We also thank Jochem De Schutter for his assistance with the toolbox `AWEbox`.

The authors used *ChatGPT* during manuscript preparation to improve text clarity and flow. All content was subsequently reviewed and edited by the authors, who take full responsibility for the publication.

https://doi.org/10.5194/wes-2025-288
Preprint. Discussion started: 9 January 2026

eawe european academy of wind energy
Open Access WIND ENERGY SCIENCE DISCUSSIONS

References

Andersson, J. A. E., Gillis, J., Horn, G., Rawlings, J. B., and Diehl, M.: CasADi – A software framework for nonlinear optimization and optimal control, Mathematical Programming Computation, 11, 1–36, https://doi.org/10.1007/s12532-018-0139-4, 2019.

Bechtle, P., Schelbergen, M., Schmehl, R., Zillmann, U., and Watson, S.: Airborne wind energy resource analysis, Renewable Energy, 141, 1103–1116, https://doi.org/https://doi.org/10.1016/j.renene.2019.03.118, 2019.

Caprace, D.-G., Winckelmans, G., and Chatelain, P.: An immersed lifting and dragging line model for the vortex particle-mesh method, Theoretical and Computational Fluid Dynamics, 34, 21–48, https://doi.org/10.1007/s00162-019-00510-1, 2020.

Cherubini, A., Papini, A., Vertechy, R., and Fontana, M.: Airborne Wind Energy Systems: A review of the technologies, Renewable and Sustainable Energy Reviews, 51, 1461–1476, https://doi.org/https://doi.org/10.1016/j.rser.2015.07.053, 2015.

Cocle, R., Bricteux, L., and Winckelmans, G.: Scale dependence and asymptotic very high Reynolds number spectral behavior of multiscale subgrid models, Physics of Fluids, 21, 085 101, https://doi.org/10.1063/1.3194302, 2009.

Coquelet, M., Moens, M., Bricteux, L., Crismer, J.-B., and Chatelain, P.: Performance assessment of wake mitigation strategies, Journal of Physics: Conference Series, 2265, 032 078, https://doi.org/10.1088/1742-6596/2265/3/032078, 2022.

Crismer, J.-B., Trigaux, F., Duponcheel, M., and Winckelmans, G.: Large-Eddy Simulation of airborne wind energy systems wakes, Journal of Physics: Conference Series, 2505, 012 036, https://doi.org/10.1088/1742-6596/2505/1/012036, 2023.

Crismer, J.-B., Haas, T., Duponcheel, M., and Winckelmans, G.: Airborne wind energy systems flying optimal trajectories in turbulent wind using flight path tracking, Journal of Physics: Conference Series, 2767, 072 021, https://doi.org/10.1088/1742-6596/2767/7/072021, 2024.

De Schutter, J., Leuthold, R., Bronnenmeyer, T., Malz, E., Gros, S., and Diehl, M.: AWEbox: An Optimal Control Framework for Single- and Multi-Aircraft Airborne Wind Energy Systems, Energies, 16, https://doi.org/10.3390/en16041900, 2023.

Dimitrov, N., Pedersen, M., and Hannesdóttir, Á.: An open-source Python-based tool for Mann turbulence generation with constraints and non-Gaussian capabilities, Journal of Physics: Conference Series, 2767, 052 058, https://doi.org/10.1088/1742-6596/2767/5/052058, 2024.

Duponcheel, M., Bricteux, L., Manconi, M., Winckelmans, G., and Bartosiewicz, Y.: Assessment of RANS and improved near-wall modeling for forced convection at low Prandtl numbers based on LES up to Re_τ=2000, International Journal of Heat and Mass Transfer, 75, 470–482, https://doi.org/10.1016/j.ijheatmasstransfer.2014.03.080, 2014.

Eijkelhof, D.: Design and Optimisation Framework of a Multi-MW Airborne Wind Energy Reference System, Delft University of Technology & Technical University of Denmark, https://resolver.tudelft.nl/uuid:e759f9ad-ab67-43b3-97e0-75558ecf222d, 2019.

Eijkelhof, D. and Schmehl, R.: Six-degrees-of-freedom simulation model for future multi-megawatt airborne wind energy systems, Renewable Energy, 196, 137–150, https://doi.org/https://doi.org/10.1016/j.renene.2022.06.094, 2022.

Fasel, U., Tiso, P., Keidel, D., Molinari, G., and Ermanni, P.: Reduced-Order Dynamic Model of a Morphing Airborne Wind Energy Aircraft, AIAA Journal, 57, 3586–3598, https://doi.org/10.2514/1.J058019, 2019.

Gros, S. and Diehl, M.: Modeling of Airborne Wind Energy Systems in Natural Coordinates, pp. 181–203, Springer Berlin Heidelberg, Berlin, Heidelberg, ISBN 978-3-642-39965-7, https://doi.org/10.1007/978-3-642-39965-7_10, 2013.

Haas, T. and Meyers, J.: Comparison study between wind turbine and power kite wakes, Journal of Physics: Conference Series, 854, 012 019, https://doi.org/10.1088/1742-6596/854/1/012019, 2017.

Haas, T., De Schutter, J., Diehl, M., and Meyers, J.: Wake characteristics of pumping mode airborne wind energy systems, Journal of Physics: Conference Series, 1256, 012 016, https://doi.org/10.1088/1742-6596/1256/1/012016, 2019.

https://doi.org/10.5194/wes-2025-288
Preprint. Discussion started: 9 January 2026

Haas, T., De Schutter, J., Diehl, M., and Meyers, J.: Large-eddy simulation of airborne wind energy farms, Wind Energy Science, 7, 1093–1135, https://doi.org/10.5194/wes-7-1093-2022, 2022.

Hagen, L. v., Petrick, K., Wilhelm, S., and Schmehl, R.: Life-Cycle Assessment of a Multi-Megawatt Airborne Wind Energy System, Energies, 16, https://doi.org/10.3390/en16041750, 2023.

Houska, B. and Diehl, M.: Optimal control for power generating kites, in: 2007 European Control Conference (ECC), pp. 3560–3567, https://doi.org/10.23919/ECC.2007.7068861, 2007.

HSL: A collection of Fortran codes for large scale scientific computation, http://www.hsl.rl.ac.uk [Accessed: 2022-07-06].

IEA – International Energy Agency: Net Zero by 2050: A roadmap for the global energy system, CC BY 4.0, Paris, 2021.

Jeanmart, H. and Winckelmans, G.: Investigation of eddy-viscosity models modified using discrete filters: A simplified "regularized variational multiscale model" and an "enhanced field model", Physics of Fluids, 19, 055 110, https://doi.org/10.1063/1.2728935, 2007.

Joshi, R., Schmehl, R., and Kruijff, M.: Power curve modelling and scaling of fixed-wing ground-generation airborne wind energy systems, Wind Energy Science, 9, 2195–2215, https://doi.org/10.5194/wes-9-2195-2024, 2024.

Malz, E., Koenemann, J., Sieberling, S., and Gros, S.: A reference model for airborne wind energy systems for optimization and control, Renewable Energy, 140, 1004–1011, https://doi.org/https://doi.org/10.1016/j.renene.2019.03.111, 2019.

Mann, J.: The spatial structure of neutral atmospheric surface-layer turbulence, Journal of Fluid Mechanics, 273, 141–168, https://doi.org/10.1017/S0022112094001886, 1994.

McCormick, B.: Aerodynamics, Aeronautics, and Flight Mechanics, Wiley, ISBN 0471575062, 1995.

Moens, M. and Chatelain, P.: Correlations Between Wake Phenomena and Fatigue Loads Within Large Wind Farms: A Large-Eddy Simulation Study, Frontiers in Energy Research, 10, https://doi.org/10.3389/fenrg.2022.881532, 2022.

Monaghan, J. J.: Extrapolating B splines for interpolation, Journal of Computational Physics, 60, 253–262, https://doi.org/https://doi.org/10.1016/0021-9991(85)90006-3, 1985.

Pynaert, N., Wauters, J., Crevecoeur, G., and Degroote, J.: Unsteady aerodynamic simulations of a multi-megawatt airborne wind energy reference system using computational fluid dynamics, Journal of Physics: Conference Series, 2265, 042 060, https://doi.org/10.1088/1742-6596/2265/4/042060, 2022.

Pynaert, N., Haas, T., Wauters, J., Crevecoeur, G., and Degroote, J.: Wing Deformation of an Airborne Wind Energy System in Crosswind Flight Using High-Fidelity Fluid–Structure Interaction, Energies, 16, https://doi.org/10.3390/en16020602, 2023.

Pynaert, N., Haas, T., Wauters, J., Crevecoeur, G., and Degroote, J.: Moving control surfaces in a geometry-resolved CFD model of an airborne wind energy system, Journal of Physics: Conference Series, 2767, 022 041, https://doi.org/10.1088/1742-6596/2767/2/022041, 2024.

Rapp, S., Schmehl, R., Oland, E., and Haas, T.: Cascaded Pumping Cycle Control for Rigid Wing Airborne Wind Energy Systems, Journal of Guidance, Control, and Dynamics, 42, 2456–2473, https://doi.org/10.2514/1.G004246, 2019.

Sánchez-Arriaga, G., Pastor-Rodríguez, A., Sanjurjo-Rivo, M., and Schmehl, R.: A lagrangian flight simulator for airborne wind energy systems, Applied Mathematical Modelling, 69, 665–684, https://doi.org/https://doi.org/10.1016/j.apm.2018.12.016, 2019.

Schelbergen, M., Kalverla, P. C., Schmehl, R., and Watson, S. J.: Clustering wind profile shapes to estimate airborne wind energy production, Wind Energy Science, 5, 1097–1120, https://doi.org/10.5194/wes-5-1097-2020, 2020.

Sommerfeld, M., Dörenkämper, M., De Schutter, J., and Crawford, C.: Impact of wind profiles on ground-generation airborne wind energy system performance, Wind Energy Science, 8, 1153–1178, https://doi.org/10.5194/wes-8-1153-2023, 2023.

https://doi.org/10.5194/wes-2025-288
Preprint. Discussion started: 9 January 2026

Sørensen, J. N. and Shen, W. Z.: Numerical Modeling of Wind Turbine Wakes, Journal of Fluids Engineering, 124, 393–399, https://doi.org/10.1115/1.1471361, 2002.

Sørensen, J. N. and Larsen, G. C.: Assessment of energy production and costs associated with a massive exploitation of wind power in the North Sea, Journal of Physics: Conference Series, 2505, 012 013, https://doi.org/10.1088/1742-6596/2505/1/012013, 2023.

Trigaux, F., Chatelain, P., and Winckelmans, G.: Investigation of blade flexibility effects on the loads and wake of a 15 MW wind turbine using a flexible actuator line method, Wind Energy Science, 9, 1765–1789, https://doi.org/10.5194/wes-9-1765-2024, 2024a.

Trigaux, F., Villeneuve, T., Dumas, G., and Winckelmans, G.: Near-tip correction functions for the actuator line method to improve the predicted lift and drag distributions, Journal of Fluid Mechanics, 989, A1, https://doi.org/10.1017/jfm.2024.461, 2024b.

Vermillion, C., Cobb, M., Fagiano, L., Leuthold, R., Diehl, M., Smith, R. S., Wood, T. A., Rapp, S., Schmehl, R., Olinger, D., and Demetriou, M.: Electricity in the air: Insights from two decades of advanced control research and experimental flight testing of airborne wind energy systems, Annual Reviews in Control, 52, 330–357, https://doi.org/https://doi.org/10.1016/j.arcontrol.2021.03.002, 2021.

Vimalakanthan, K., Caboni, M., Schepers, J., Pechenik, E., and Williams, P.: Aerodynamic analysis of Ampyx's airborne wind energy system, Journal of Physics: Conference Series, 1037, 062 008, https://doi.org/10.1088/1742-6596/1037/6/062008, 2018.

Wächter, A. and Biegler, L. T.: On the implementation of an interior-point filter line-search algorithm for large-scale nonlinear programming, Mathematical Programming, 106, 25–57, https://doi.org/10.1007/s10107-004-0559-y, 2006.

Watson, S., Moro, A., Reis, V., Baniotopoulos, C., Barth, S., Bartoli, G., Bauer, F., Boelman, E., Bosse, D., Cherubini, A., Croce, A., Fagiano, L., Fontana, M., Gambier, A., Gkoumas, K., Golightly, C., Latour, M. I., Jamieson, P., Kaldellis, J., Macdonald, A., Murphy, J., Muskulus, M., Petrini, F., Pigolotti, L., Rasmussen, F., Schild, P., Schmehl, R., Stavridou, N., Tande, J., Taylor, N., Telsnig, T., and Wiser, R.: Future emerging technologies in the wind power sector: A European perspective, Renewable and Sustainable Energy Reviews, 113, 109 270, https://doi.org/https://doi.org/10.1016/j.rser.2019.109270, 2019.

Wijnja, J., Schmehl, R., De Breuker, R., Jensen, K., and Vander Lind, D.: Aeroelastic Analysis of a Large Airborne Wind Turbine, Journal of Guidance, Control, and Dynamics, 41, 2374–2385, https://doi.org/10.2514/1.G001663, 2018.